

CHANDRA OBSERVATIONS OF THE CL1604 SUPERCLUSTER AT $z = 0.9$: EVIDENCE FOR AN OVERDENSITY OF ACTIVE GALACTIC NUCLEI

DALE D. KOCEVSKI¹, LORI M. LUBIN¹, ROY GAL², BRIAN C. LEMAUX¹, CHRISTOPHER D. FASSNACHT¹, AND GORDON K. SQUIRES³

¹ Department of Physics, University of California, Davis, 1 Shields Avenue, Davis, CA 95616, USA; kocevski@physics.ucdavis.edu

² Institute for Astronomy, University of Hawaii, 2680 Woodlawn Dr., Honolulu, HI 96822, USA

³ *Spitzer* Science Center, M/S 220-6, California Institute of Technology, 1200 East California Blvd., Pasadena, CA 91125, USA

Received 2008 April 11; accepted 2008 August 11; published 2008 December 1

ABSTRACT

We present the results of *Chandra* observations of the CL1604 supercluster at $z \sim 0.9$. The system is the largest structure mapped at redshifts approaching unity, containing at least eight spectroscopically confirmed galaxy clusters and groups. Using two 50 ks ACIS-I pointings we examine both the X-ray point-source population and the diffuse emission from individual clusters in the system. Over an area encompassing the entire supercluster ($\sim 0.154 \text{ deg}^2$), we find a 2.5σ excess of point sources detected in the hard band (2–10 keV) relative to the number of sources found in blank fields observed by *Chandra*. No such excess is observed in the soft band (0.5–2 keV). The hard-band source density is 1.47 times greater than that of a blank field, in agreement with the previously reported correlation between overdensity amplitude and cluster redshift. Using a maximum likelihood technique, we have matched 112 of the 161 detected X-ray point sources to optical counterparts and found 15 sources that are associated with the supercluster. All 15 sources have rest-frame luminosities consistent with emission from active galactic nuclei (AGNs). We find that the supercluster AGNs largely avoid the densest regions of the system and are instead distributed on the outskirts of massive clusters or within poorer clusters and groups. We have also detected diffuse emission from two of the eight clusters and groups in the system, clusters CL1604 + 4304 and CL1604 + 4314. The systems have bolometric luminosities of 1.43×10^{44} and $8.20 \times 10^{43} h_{70}^{-2} \text{ erg s}^{-1}$ and gas temperatures of $3.50_{-1.08}^{+1.82}$ and $1.64_{-0.45}^{+0.65}$ keV, respectively. Using updated velocity dispersions, we compare the properties of these systems with the cluster scaling relations followed by other X-rays and optically selected galaxy clusters at high redshift.

Key words: galaxies: clusters: general – large-scale structure of universe – X-rays: galaxies: clusters

Online-only material: color figures, machine-readable tables

1. INTRODUCTION

There is an ongoing debate as to whether active galactic nuclei (AGNs) are triggered in the environments around galaxy clusters in excess to what is observed in the field. A growing number of studies have reported an overdensity of X-ray point sources in the vicinity of clusters relative to blank-field observations (Henry & Briel 1991; Cappi et al. 2001; Pentericci et al. 2002; Molnar et al. 2002; Johnson et al. 2003; D’Elia et al. 2004; Ruderman & Ebeling 2005; Cappelluti et al. 2005; Hudaverdi et al. 2006; Branchesi et al. 2007), while other studies such as the large *Chandra* archival program ChaMP (Kim et al. 2004a), using observations covering 1.1 deg^2 , find no significant difference between cluster and cluster-free fields (Molnar et al. 2002; Kim et al. 2004b).

Many studies which have reported overdensities find evidence that the excess sources are AGNs on the outskirts of clusters and that they may trace the large-scale structure which surrounds the systems. D’Elia et al. (2004) found an asymmetric distribution of point sources around the $z = 0.46$ cluster 3C 295, which the authors propose may trace a large-scale filament connected to the cluster. Johnson et al. (2003) reported a 2σ overdensity of AGNs in MS1054 – 0321 and found that the sources were preferentially located 1–2 Mpc from the cluster center. Likewise, Ruderman & Ebeling (2005) reported a statistical excess of AGNs near the virial radius of clusters after combining the source counts of 51 high-redshift clusters from the Massive Cluster Survey (MACS; Ebeling et al. 2001a).

There is also evidence that the amplitude of the observed source overdensity increases with redshift. Cappelluti et al. (2005) recently performed the first systematic search for X-ray point-source overdensities in the fields of 10 high-redshift ($0.24 < z < 1.2$) clusters observed with *Chandra*. They found that 40% of the cluster fields showed an excess of point sources and noted a correlation between the amplitude of the overdensity in the hard band and cluster redshift. A similar conclusion was reached by Branchesi et al. (2007) who examined the fields of 18 distant clusters ($0.25 < z < 1.1$). Such a correlation would be expected if AGNs are indeed tracing the cosmic web near clusters, since numerical simulations tell us that a greater degree of large-scale structure should exist around dynamically younger clusters at high redshift (Colberg et al. 2000; Evrard et al. 2002).

The findings that AGNs may trace the filaments which feed clusters are consistent with studies that suggest the large-scale structure surrounding clusters plays a pivotal role in driving galaxy evolution. Studies at low redshift have found that regions of intermediate density, such as the groups and filaments on the outskirts of clusters, already exhibit signs of galaxy transformation and reduced star-formation rates (Lewis et al. 2002; Gómez et al. 2003). Many of the processes which have been proposed to drive this evolution, such as galaxy mergers (Barnes & Hernquist 1991) and galaxy harassment (Moore et al. 1996), may also work to funnel gas to the central regions of galaxies initiating AGN activity.

Thus far it has been difficult to conclusively establish whether AGNs are triggered near clusters and to determine the processes

which may be responsible because the observed overdensities are relatively mild, resulting in a limited number of confirmed, optically identified cluster AGNs available for study in a single system. Superclusters offer an alternative to studying individual clusters or the AGN population of a statistical sample of clusters. These large-scale systems are comprised of several galaxy clusters and groups connected by a rich network of filamentary structure on scales of 10–100 Mpc (Bahcall & Soneira 1984; Einasto et al. 2001), thus potentially providing large samples of AGNs at the same epoch. Such systems not only provide significant large-scale structure within which AGN may be preferentially found, but also a wide variety of environments and local conditions to help constrain the mechanisms most responsible for triggering their activity.

Recently, Gilmour et al. (2007) used *XMM-Newton* observations of the Abell 901/902 supercluster at $z = 0.17$ to examine the environments and optical properties of X-ray-selected AGNs in the system. The authors find that AGNs are more prevalent in clusters than optical studies have suggested, in agreement with the results of Martini et al. (2002, 2006). They also note that AGN host galaxies are preferentially found in areas of modest galaxy density and strongly avoid the densest regions of the supercluster, concluding that there are strong correlations between AGN activity and local environment. Furthermore, they find that the local densities and optical colors of the AGN host galaxies are more comparable to galaxy groups and the outskirts of clusters than filament and cluster-like environments.

While low-redshift superclusters like Abell 901/902 have been well cataloged (Bahcall & Soneira 1984; Tully et al. 1992; Einasto et al. 2001) and studied for some time (e.g., Shapley 1930), only a limited number of such systems are known at higher redshifts. These include a structure at $z = 0.89$ detected in the UK Infrared Deep Survey (UKIDSS; Swinbank et al. 2007), the RCS2319 + 00 supercluster of three X-ray luminous clusters at $z = 0.9$ (Gilbank et al. 2008), and the Lynx system at $z = 1.27$ which contains at least two clusters (Nakata et al. 2005).

In this paper, we report on *Chandra* observations of the Cl1604 supercluster at $z = 0.9$. The system is the largest supercluster mapped at redshifts approaching unity, with the most constituent clusters and groups and the largest number of spectroscopically confirmed member galaxies. We here make use of two 50 ks pointings to examine both the diffuse emission from the system's clusters and the properties of point sources in the two fields.

Originally detected as two rich clusters in the optical survey of Gunn et al. (1986), follow-up wide field imaging of the Cl1604 system revealed 10 distinct red-galaxy overdensities within a $25' \times 25'$ region on the sky (Lubin et al. 2000; Gal & Lubin 2004). Extensive spectroscopic observations confirmed that four of these overdensities were galaxy clusters with velocity dispersion greater than 500 km s^{-1} , while an additional four were found to be poorer clusters and/or groups ($\sigma = 300\text{--}500 \text{ km s}^{-1}$; Postman et al. 1998, 2001; Gal et al. 2005, 2008). Thus far over 1100 secure extragalactic redshifts have been compiled in the field of the Cl1604 system, resulting in spectra for 417 confirmed supercluster members (Gal et al. 2008).

The richest cluster in the system, Cl1604 + 4304, was previously observed with *XMM-Newton* by Lubin et al. (2004), who found the system to have a bolometric luminosity of $L_x^{\text{bol}} = 2.01 \times 10^{44} h_{70}^{-2} \text{ erg s}^{-1}$ and a temperature of $T = 2.51^{+1.05}_{-0.69} \text{ keV}$. The second cluster originally detected by Gunn et al. (1986),

Table 1
Summary of Observations

Target	Obs ID	Exp. (s)	Obs. Date	Detector
Cl1604-North	6933	26691	2006 Jun 25	ACIS-I0123
Cl1604-North	7343	19412	2006 Jun 23	ACIS-I0123
Cl1604-South	6932	49478	2006 Oct 1	ACIS-I0123

Cl1604 + 4321, was not detected in *ROSAT* observations of the system and has a 3σ luminosity upper limit in the 0.1–2.4 keV band of $L_x \leq 4.76 \times 10^{43} h_{70}^{-2} \text{ erg s}^{-1}$ (Castander et al. 1994; Postman et al. 2001). The remaining six newly discovered clusters and groups in the supercluster have not been previously observed at X-ray wavelengths. Five of these systems fall within the field of view (FOV) of the *Chandra* observations presented here.

This study of the Cl1604 supercluster is organized as follows: in Section 2 we describe the X-ray observations and our data reduction procedures, as well as a summary of the optical imaging and the extensive spectroscopic data set available for the system. Section 3 discusses the properties of the detected X-ray point sources, including their log N –log S distribution, optical counterparts and redshift distribution. In Section 4, we present the X-ray luminosities and gas temperatures of the diffuse cluster emission detected in the system, followed by a comparison of the cluster X-ray properties with cluster scaling relations. Throughout this paper, we assume a Λ CDM cosmology with $\Omega_m = 0.3$, $\Omega_\Lambda = 0.7$, and $H_0 = 70 h_{70} \text{ km s}^{-1} \text{ Mpc}^{-1}$.

2. OBSERVATIONS AND DATA REDUCTION

2.1. X-Ray Observations

Observations of the Cl1604 supercluster were carried out with *Chandra's* Advanced CCD Imaging Spectrometer (ACIS; Garmire et al. 2003) on 2006 June 23 (obsID 7343), June 25 (obsID 6933), and October 1 (obsID 6932). A summary of the observational parameters of the three data sets is listed in Table 1. The three observations consist of two pointings, one encompassing the northern portion of the system and the other the southern portion, with a $4.9'$ overlap between the imaged regions. The aim points of the observations are $\alpha_{2000} = 16^{\text{h}}04^{\text{m}}12^{\text{s}}.0$, $\delta_{2000} = +43^\circ22'35''$ and $\alpha_{2000} = 16^{\text{h}}04^{\text{m}}19^{\text{s}}.5$, $\delta_{2000} = +43^\circ10'31''$. Imaging of the northern pointing was split between two observations (obsID 7343 and 6933) with nearly identical aim points and roll angles, while the southern pointing was covered by a single observation (obsID 6932). Each pointing was imaged with the $16.9' \times 16.9'$ ACIS-I array, with the aim point located on the ACIS-I3 chip. The ACIS-S2 chip was also active during the observations but due to its large off-axis angle and reduced effective area we do not make use of it in this analysis. All three observations were carried out in the VFaint telemetry mode with the nominal 3.2 s CCD frame time for a total integration of 19.4, 26.7, and 49.5 ks for the 7343, 6933, and 6932 data sets, respectively. An examination of light curves produced in the 0.3–10 keV band shows no indication of flaring during the course of the observations.

All three data sets were reprocessed and analyzed using standard CIAO 3.3 software tools and version 3.2.2 of the *Chandra* calibration database available through *Chandra* X-ray Center (CXC).⁴ New level 1 event files were produced

⁴ <http://cxc.harvard.edu/>

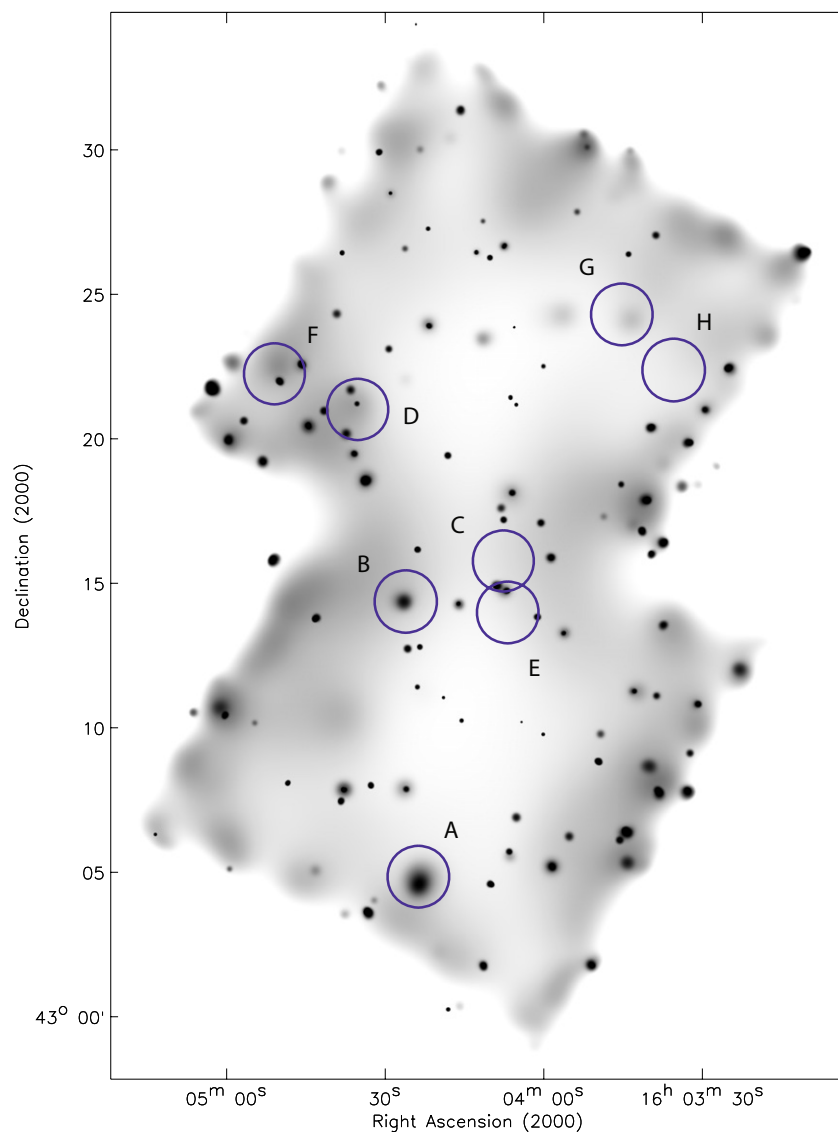


Figure 1. Adaptively smoothed, exposure-corrected mosaic of the CL1604 supercluster in the soft band (0.5–2 keV). All sources are significant to at least the 3σ level. The locations of eight red-galaxy overdensities, seven of which are spectroscopically confirmed galaxy clusters or groups in the supercluster, are circled and labeled following the naming convention of Gal et al. (2008) and that of Table 5. The circles have a radius of $0.5 h_{70}^{-1}$ Mpc at the cluster redshifts.

(A color version of this figure is available in the online journal.)

using the `acis_process_events` script, which makes use of the latest gain files and corrects for the effects of time-dependent variations and charge transfer inefficiencies (CTIs) in the ACIS CCDs. Level 2 event files were produced by filtering on standard *ASCA* grades (grades = 0, 2, 3, 4, 6), good status bits (status = 0), and good time intervals (GTIs) supplied by the pipeline. We checked the relative astrometry between the three event files using the positions of 14 high signal-to-noise sources in the overlap region between the two pointings and found the astrometric errors to be negligible. Images for use in object detection and the examination of extended cluster emission were created from the event lists in the 0.5–2 keV (soft), 2–8 keV (hard), and 0.5–8 keV (full) X-ray bands with the standard $0''.492$ pixel $^{-1}$ binning. To account for vignetting, CCD gaps, and telescope dither effects, we created spectrally weighted, energy-dependent exposure maps in each of the three bands assuming a power-law source spectrum with a photon index set to the slope of the X-ray background in the 0.5–8 keV band, $\gamma = 1.4$ (Tozzi et al. 2001; Kushino et al. 2002).

An adaptively smoothed, exposure-corrected mosaic of the CL1604 supercluster in the soft band is shown in Figure 1. The mosaic was constructed by reprojecting each event file to the tangent point $\alpha_{2000} = 16^{\text{h}}04^{\text{m}}12^{\text{s}}.4$, $\delta_{2000} = +43^{\circ}16'18''$ with the `reproject_events` task in CIAO and combining the resulting files. Exposure variations and vignetting were corrected by using a composite exposure map constructed by reprojecting and combining our individual exposure maps with the `reproject_image_grid` task.

It should be noted that since the aim points and roll angles for the 7343 and 6933 observations are nearly identical, we have reprojected and combined the images and exposure maps of these pointings and treat the combination as a single observation throughout our analysis. Hereafter, we refer to the composite pointing as CL1604-North, while the 6932 observation will be referred to as CL1604-South. Also, in what follows we largely work separately with the CL1604-North and CL1604-South data sets as opposed to the composite mosaic.

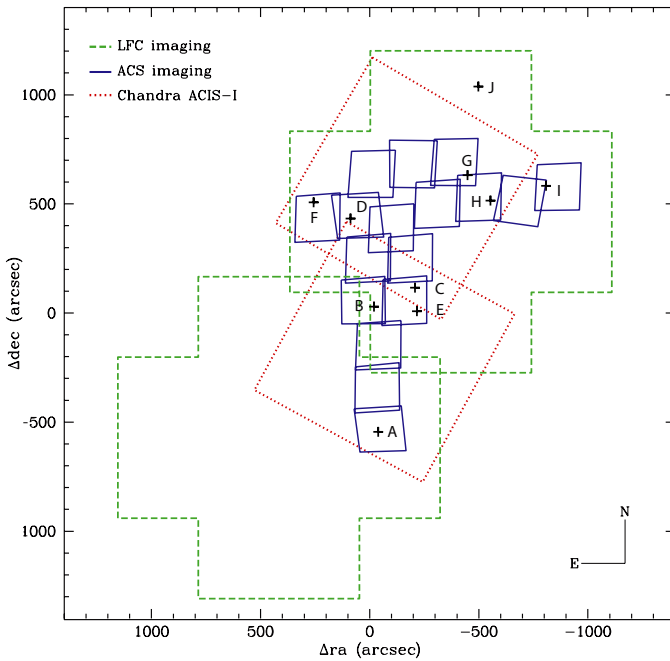


Figure 2. Positions and FOVs of the two LFC, two ACIS-I, and 17 ACS pointings in the Cl1604 region. The positions of the ten red-galaxy overdensities found by Gal et al. (2005, 2008) are marked and labeled following the naming convention of Table 5.

2.2. Optical Imaging

Our optical data of the system consist of two pointings of the Large Format Camera (LFC) on the Palomar 5 m telescope and 17 pointings of the higher-resolution Advanced Camera for Surveys (ACS) on the *Hubble Space Telescope* (HST). Details of these observations and subsequent data reduction are presented in Gal et al. (2005, 2008) and D. D. Kocevski et al. (2008, in preparation) and are only briefly discussed here.

The LFC is a mosaic camera of six 2048×4096 CCDs with a pixel scale of $0''.182 \text{ pixel}^{-1}$, resulting in an unvignetted FOV that is roughly circular with a $24'$ diameter. We imaged two pointings in the field of Cl1604 using the Sloan Digital Sky Survey (SDSS) r' , i' , and z' filters, reaching a depth of 24.4, 24.2, and 23.2 mag in each band, respectively. The area imaged by the two LFC pointings relative to our ACIS-I imaging is shown in Figure 2. The ACS camera consists of two 2048×4096 CCDs with a pixel scale of $0''.05 \text{ pixel}^{-1}$, resulting in a $\sim 3' \times 3'$ FOV. Our ACS imaging is comprised of a 17 pointing mosaic designed to image nine of the ten galaxy density peaks observed in our LFC imaging of the supercluster. An outline of the mosaic is shown in Figure 2. Observations were taken in both the F606W and F814W bands, resulting in completeness depths of ~ 26.5 mag in each band. The astrometry of the 17 pointings was fixed to that of the USNO-B catalog (Monet et al. 2003) so as to match our LFC imaging, and the final images were resampled to a pixel scale of $0''.03 \text{ pixel}^{-1}$. Source catalogs were produced from both the LFC and ACS imaging in each of the five bands observed using the Source Extractor (SExtractor) routine (Bertin & Arnouts 1996) and cross-correlated to produce a single, composite optical catalog. An outline of the region covered by our optical imaging relative to the ACIS-I observations is shown in Figure 2.

2.3. Optical Spectroscopy

The Cl1604 supercluster has been extensively mapped using the Low-Resolution Imaging Spectrograph (LRIS; Oke et al. 1995) and the Deep Imaging Multi-Object Spectrograph (DEIMOS; Faber et al. 2003) on the Keck 10 m telescopes (Oke et al. 1998; Postman et al. 1998; Lubin et al. 1998; Gal & Lubin 2004; Gal et al. 2008). The complex target selection, spectral reduction, and redshift measurements are described in detail in Section 3 of Gal et al. (2008). The final spectroscopic catalog contains 1671 unique objects. Redshifts derived for these objects are given a spectroscopic quality, Q_{spect} , between 1 and 4, where 1 indicates that a secure redshift could not be determined due to poor signal, lack of features or reduction artifacts, 2 is a redshift obtained from either a single feature or two marginally detected features, 3 is a redshift derived from at least one secure and one marginal feature, and 4 is assigned to spectra with redshifts obtained from several high signal-to-noise features. A value of $Q_{\text{spect}} = -1$ is used for sources securely identified as stars.

In this sample, we find 140 stars and 1138 extragalactic objects with $Q_{\text{spect}} \geq 3$. A total of 417 galaxies are in the nominal redshift range of the supercluster between $0.84 \leq z \leq 0.96$. This extensive spectroscopic database is larger by a factor of ~ 10 than that for any other known moderate-to-high-redshift supercluster.

3. POINT-SOURCE PROPERTIES AND NUMBER COUNTS

3.1. Object Detection and Photometry

We searched for X-ray point sources in the field of Cl1604 using the wavelet-based *wavdetect* procedure in CIAO. We employed the standard $\sqrt{2}^i$ series of wavelet pixel scales, with $i = 0-16$. These scales are the radius of a Mexican hat function in pixels with one pixel = $0''.492$. We also adopted a minimum exposure threshold of 20% relative to the exposure at the aim point of the observation and a threshold significance for spurious detections of 10^{-6} . The latter implies less than one false detection per ACIS chip (which contains 1024×1024 pixels at full resolution), or roughly eight false detections over our entire FOV (Freeman et al. 2002). Object detection was carried out on the unvignetted-corrected, full resolution images of the northern and southern pointings separately and in each of the soft, hard and full X-ray bands. The positions of the detected sources were then cross-correlated to produce a multi-band source list for each pointing. We set the final position of each source in this composite list to the measured position in the band within which the source was detected with the greatest significance. With no cut on significance, we detect a total of 99, 49, and 93 point sources in the soft, hard, and full bands, respectively, in the northern pointing, and 117, 54, and 105 sources in the same bands for the southern pointing. Our detections are summarized in Table 2. In total, 265 unique sources were detected in the two pointings of the Cl1604 system, of which 161 had detection significances greater than 3σ in at least one X-ray band.

We tested the stability of our object detection procedure using sources found in the $4''.9$ overlap region between the northern and southern pointings of the Cl1604 field. We found the procedure to be robust for sources detected with relatively high significance and moderate off-axis angles. Only a single source detected at the 5σ level is not detected in both the northern and southern pointings separately. This increases to five sources at the 3σ

Table 2
Point-Source Detections in the Cl1604 Supercluster

Cl1604 Pointing	Soft ^a All (3 σ)	Hard ^b All (3 σ)	Full ^c All (3 σ)	Total Uniq. All (3 σ) ^d
North	99 (66)	49 (44)	93 (75)	123 (85)
South	117 (67)	54 (42)	105 (75)	147 (90)
North+South	203 (120)	94 (77)	184 (136)	256 (161)

Notes.

^a 0.5–2 keV.

^b 2–8 keV.

^c 0.5–8 keV.

^d 3 σ detection in at least one band.

level, but these are largely located near the boundaries of one of the two pointings where the off-axis angle is large and the point-spread function (PSF) has degraded considerably.

The properties of the detected point sources, including count rates and detection significances, were determined with follow-up aperture photometry on all sources found by *wavdetect*. The apertures used were defined so as to contain 95% of the flux from a given point source. As the *Chandra* PSF is dependent on both energy and off-axis angle, we determined the 95% enclosed energy radius, R_{95} , at the position of each source using the PSF libraries in the *Chandra* calibration database. This was done at 1.49 and 4.51 keV for photometry in the soft and hard bands, respectively. The radius of the resulting apertures at 1.49 keV ranged from 1''.8 on-axis to 15''.8 at 12'.1 off-axis, the distance of our most off-axis source; the latter increased to 17''.2 at 4.51 keV. The background near each source was determined in an annulus extending from 1.2 to $2.4 \times R_{95}$, with appropriate masking of nearby sources when necessary. We carried out the photometry on the vignetting-corrected, soft- and hard-band images of both pointings, and an aperture correction of 1/0.95 was applied to the background-subtracted net counts of each source. Counts in the full band were then determined as a sum of the measured net counts in the soft and hard bands. We again tested the stability of our photometry using sources located in the overlap region and found that the variations in the source counts measured in the two pointings were consistent with the expected level of Poissonian noise.

As the low number of counts for many of the detected sources are not favorable to a full spectroscopic analysis, we determined the soft- and hard-band fluxes of each source by normalizing a power-law spectral model to the net count rate measured for each source. These rates were determined by dividing the net counts measured in the vignetting-corrected images by the nominal exposure time at the aim point of each observation. We assumed a photon index of $\gamma = 1.4$ for the power-law model and a Galactic neutral hydrogen column density of $1.21 \times 10^{20} \text{ cm}^{-2}$ (Dickey & Lockman 1990), resulting in a count rate to unabsorbed-flux conversion factor of 5.85×10^{-12} and $2.08 \times 10^{-11} \text{ erg cm}^{-2} \text{ s}^{-1}$ per cnts s^{-1} in the soft and hard bands, respectively.⁵ Full-band fluxes were again determined by summing the flux in the soft and hard bands.

Properties for the 161 unique sources detected with at least a 3 σ significance in the field of Cl1604 are listed in Table 3. The table includes source IDs (Column 1), right ascensions and declinations (Columns 2 and 3), positional errors determined using the empirical relationships of Kim et al. (2007; Column 4),

⁵ It is worth noting that the count rate to flux conversion is not significantly affected by the assumed power-law index. For example, a change of 0.1 in γ results in only a $\sim 2\%$ change in the soft-band conversion factor.

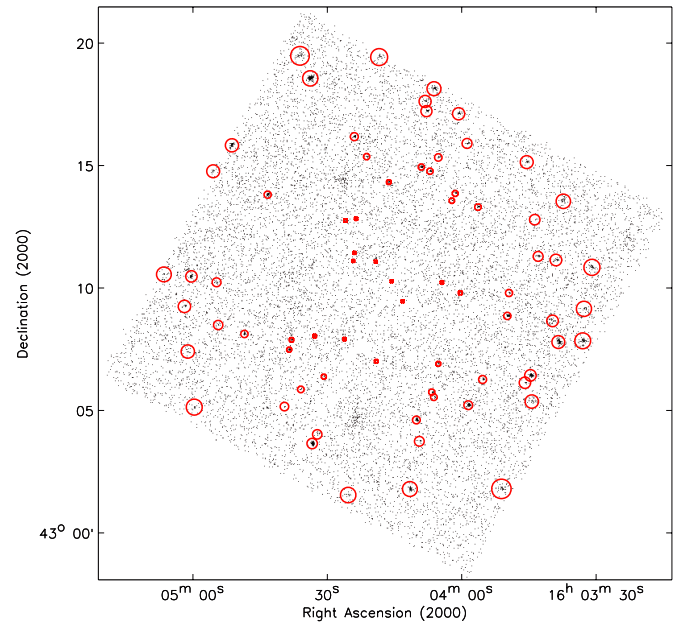


Figure 3. Apertures containing 95% of the flux from point sources detected in the Cl1604-South pointing with a 3 σ significance in the 0.5–2 keV band. The radius has been calculated at an energy of 1.49 keV. The underlying soft-band image has been binned to a pixel scale of $2'' \text{ pixel}^{-1}$.

(A color version of this figure is available in the online journal.)

aperture-corrected, net counts above the background in the soft, hard and full bands (Columns 5–7), X-ray fluxes in all three bands in units of $\text{erg s}^{-1} \text{ cm}^{-2}$ (Columns 8–10), detection significances measured as

$$\text{sig} = \text{net_cnts} / \left(1.0 + \sqrt{0.75 + \text{bkg_cnts}} \right) \quad (1)$$

(Columns 11–13), hardness ratios measured as $\text{HR} = (H - S) / (H + S)$ where H and S are the net counts in the hard and soft bands, respectively (Column 14), and a three-letter string indicating the bands in which the source was detected using *wavdetect*, with S, H and F indicating the soft, hard and full bands, respectively (Column 15).

3.2. Log N –Log S

To investigate whether an excess of unresolved X-ray sources exists in the field of Cl1604 relative to fields without such a structure, we have calculated the cumulative source number counts, $N(>S)$, as described by Gioia et al. (1990) using

$$N(>S) = \sum_{i=1}^N \frac{1}{\Omega_i} \text{deg}^{-2}. \quad (2)$$

Here, N is the total number of detected point sources and Ω_i is the sky area in square degrees sampled by the detector down to the flux of the i th source. The variance of the number counts was in turn calculated as

$$\sigma_i^2 = \sum_{i=1}^N \left(\frac{1}{\Omega_i} \right)^2. \quad (3)$$

Determining Ω_i for a given *Chandra* observation is complicated by the fact that the flux limit across the ACIS-I array varies due to vignetting and PSF degradation as a function of

Table 3
Catalog of the 161 X-Ray Sources Detected in the Field of the Cl1604 Supercluster with a 3σ Significance in at Least One X-Ray Band

Source Name	R.A. (J2000)	Decl. (J2000)	Error ($''$)	(Soft)	Net Cnts ^a (Hard)	(Full)	(Soft)	F_x^b (Hard)	(Full)	(Soft)	Sig ^c (Hard)	(Full)	HR	Wavdetect ^d Flag
J160310.5+432627	16:03:10.5	43:26:27.3	4.83	99.4	80.9	180.3	1.26×10^{-14}	3.57×10^{-14}	4.82×10^{-14}	20.4	13.4	25.1	-0.10	SHF
J160316.9+432256	16:03:16.9	43:22:56.3	5.26	5.8	23.4	29.1	7.29×10^{-16}	1.03×10^{-14}	1.10×10^{-14}	1.5	4.6	4.9	0.60	HF
J160320.4+431220	16:03:20.4	43:12:20.2	9.27	9.1	13.8	22.9	1.10×10^{-15}	6.06×10^{-15}	7.16×10^{-15}	2.0	2.2	3.2	0.21	SF
J160324.9+432226	16:03:24.9	43:22:26.2	2.01	73.2	27.9	101.0	9.25×10^{-15}	1.23×10^{-14}	2.15×10^{-14}	23.3	6.5	21.7	-0.45	SHF
J160329.4+432059	16:03:29.4	43:20:59.5	2.73	24.6	11.7	36.3	3.11×10^{-15}	5.14×10^{-15}	8.25×10^{-15}	8.2	3.0	8.5	-0.36	SF
J160330.7+431049	16:03:30.7	43:10:49.9	2.68	30.5	23.5	54.0	3.70×10^{-15}	1.03×10^{-14}	1.40×10^{-14}	8.0	4.4	9.0	-0.13	SHF
J160332.4+431953	16:03:32.4	43:19:53.1	1.66	47.7	28.2	75.9	6.03×10^{-15}	1.24×10^{-14}	1.85×10^{-14}	15.9	7.3	17.7	-0.26	SF
J160332.5+430908	16:03:32.5	43:09:08.4	4.48	14.6	0.0	14.6	1.76×10^{-15}	0.00	1.76×10^{-15}	3.8	0.0	2.6	-1.00	SF
J160332.8+430750	16:03:32.8	43:07:50.2	2.18	45.3	39.8	85.1	5.48×10^{-15}	1.75×10^{-14}	2.30×10^{-14}	13.8	8.0	15.8	-0.06	SHF
J160336.9+431906	16:03:36.9	43:19:06.8	4.01	11.2	6.3	17.5	1.42×10^{-15}	2.77×10^{-15}	4.19×10^{-15}	4.1	1.7	4.5	-0.28	S
J160337.1+431331	16:03:37.1	43:13:31.6	4.50	23.6	12.7	36.3	2.86×10^{-15}	5.57×10^{-15}	8.44×10^{-15}	6.5	2.7	6.8	-0.30	SF
J160337.3+431625	16:03:37.3	43:16:25.3	2.27	51.6	24.8	76.4	6.52×10^{-15}	1.09×10^{-14}	1.75×10^{-14}	16.6	5.9	16.6	-0.35	SHF
J160338.3+430747	16:03:38.3	43:07:47.3	1.15	91.5	61.9	153.5	1.11×10^{-14}	2.73×10^{-14}	3.84×10^{-14}	26.7	13.3	29.7	-0.19	SHF
J160338.8+431108	16:03:38.8	43:11:08.0	3.10	17.1	2.2	19.3	2.07×10^{-15}	9.67×10^{-16}	3.04×10^{-15}	5.7	0.5	4.3	-0.77	SF
J160338.8+432702	16:03:38.8	43:27:02.7	3.56	10.2	6.1	16.3	1.29×10^{-15}	2.70×10^{-15}	3.98×10^{-15}	3.5	1.4	3.6	-0.25	SF
J160339.2+431902	16:03:39.2	43:19:02.8	2.96	9.7	0.8	10.5	1.23×10^{-15}	3.68×10^{-16}	1.59×10^{-15}	3.7	0.2	2.9	-0.84	SF
J160339.6+430839	16:03:39.6	43:08:39.1	4.67	14.4	9.4	23.7	1.74×10^{-15}	4.12×10^{-15}	5.86×10^{-15}	4.6	2.4	5.4	-0.21	F
J160339.6+431601	16:03:39.6	43:16:01.1	2.26	38.4	31.8	70.2	4.85×10^{-15}	1.40×10^{-14}	1.89×10^{-14}	11.4	6.8	13.5	-0.09	SHF
J160339.7+432023	16:03:39.7	43:20:23.7	0.89	67.1	22.5	89.7	8.48×10^{-15}	9.94×10^{-15}	1.84×10^{-14}	26.6	7.2	26.9	-0.50	SHF
J160340.2+430853	16:03:40.2	43:08:53.8	3.33	6.2	11.1	17.3	7.53×10^{-16}	4.88×10^{-15}	5.64×10^{-15}	2.1	2.9	4.0	0.28	HF
J160340.6+431752	16:03:40.6	43:17:52.4	1.12	88.5	40.5	129.0	1.12×10^{-14}	1.79×10^{-14}	2.91×10^{-14}	29.6	10.5	30.4	-0.37	SHF
J160341.4+431649	16:03:41.4	43:16:49.8	1.57	43.6	34.8	78.4	5.51×10^{-15}	1.53×10^{-14}	2.08×10^{-14}	13.3	7.7	15.8	-0.11	SHF
J160342.8+431117	16:03:42.8	43:11:17.0	3.09	18.1	0.0	18.1	2.19×10^{-15}	0.00	2.19×10^{-15}	5.9	0.0	4.6	-1.00	S
J160343.5+431246	16:03:43.5	43:12:46.9	2.94	8.7	4.0	12.7	1.05×10^{-15}	1.75×10^{-15}	2.81×10^{-15}	3.0	1.0	3.0	-0.37	SF
J160343.7+433007	16:03:43.7	43:30:07.3	5.55	45.0	20.7	65.7	5.69×10^{-15}	9.12×10^{-15}	1.48×10^{-14}	14.1	4.8	14.0	-0.37	F
J160343.8+432622	16:03:43.8	43:26:22.7	1.57	15.1	18.5	33.6	1.91×10^{-15}	8.16×10^{-15}	1.01×10^{-14}	5.7	5.7	9.4	0.10	SHF
J160344.2+430521	16:03:44.2	43:05:21.9	4.24	15.2	11.3	26.5	1.84×10^{-15}	4.99×10^{-15}	6.83×10^{-15}	4.6	2.4	5.2	-0.14	F
J160344.5+430625	16:03:44.5	43:06:26.0	1.18	148.5	83.5	232.0	1.80×10^{-14}	3.68×10^{-14}	5.47×10^{-14}	46.4	19.1	48.3	-0.28	SHF
J160345.3+431507	16:03:45.3	43:15:07.7	3.28	12.8	7.9	20.7	1.55×10^{-15}	3.46×10^{-15}	5.01×10^{-15}	3.9	1.9	4.5	-0.24	SF
J160345.3+431824	16:03:45.3	43:18:24.9	2.64	14.9	5.6	20.5	1.88×10^{-15}	2.47×10^{-15}	4.36×10^{-15}	6.0	1.7	6.0	-0.45	SF
J160345.5+432328	16:03:45.5	43:23:28.6	2.70	7.3	0.0	7.3	9.24×10^{-16}	0.00	9.24×10^{-16}	3.1	0.0	2.5	-1.00	S
J160345.8+430608	16:03:45.8	43:06:08.0	3.86	11.5	0.1	11.6	1.40×10^{-15}	3.12×10^{-17}	1.43×10^{-15}	3.8	0.0	2.6	-0.99	SF
J160348.8+431717	16:03:48.8	43:17:17.3	2.96	8.1	6.1	14.1	1.02×10^{-15}	2.67×10^{-15}	3.69×10^{-15}	2.9	1.7	3.6	-0.14	SF

Table 3
(Continued)

Source Name	R.A. (J2000)	Decl. (J2000)	Error (")	(Soft)	Net Cnts ^a (Hard)	(Full)	(Soft)	F_x^b (Hard)	(Full)	(Soft)	Sig ^c (Hard)	(Full)	HR	Wavdetect ^d Flag
J160349.3+430947	16:03:49.3	43:09:47.6	2.87	9.5	6.9	16.3	1.15×10^{-15}	3.02×10^{-15}	4.17×10^{-15}	3.8	2.2	5.0	-0.16	S
J160349.7+430851	16:03:49.7	43:08:51.4	0.60	128.8	46.1	174.9	1.56×10^{-14}	2.03×10^{-14}	3.59×10^{-14}	50.5	14.4	51.3	-0.47	SHF
J160350.8+432123	16:03:50.8	43:21:23.1	1.37	1.2	17.8	19.1	1.55×10^{-16}	7.87×10^{-15}	8.02×10^{-15}	0.6	7.0	7.2	0.87	HF
J160351.1+430148	16:03:51.1	43:01:48.3	3.89	43.5	29.2	72.6	5.27×10^{-15}	1.28×10^{-14}	1.81×10^{-14}	11.0	5.0	11.2	-0.20	SF
J160351.5+433007	16:03:51.5	43:30:07.7	4.59	13.3	17.5	30.9	1.68×10^{-15}	7.73×10^{-15}	9.42×10^{-15}	3.6	3.4	5.4	0.14	SF
J160353.7+432752	16:03:53.7	43:27:52.2	2.71	8.3	5.5	13.8	1.05×10^{-15}	2.42×10^{-15}	3.47×10^{-15}	3.4	1.7	4.0	-0.21	SF
J160354.7+432105	16:03:54.7	43:21:05.8	1.67	1.1	6.8	7.9	1.43×10^{-16}	2.98×10^{-15}	3.13×10^{-15}	0.6	3.0	3.4	0.71	HF
J160355.2+430616	16:03:55.2	43:06:16.0	1.43	13.3	24.2	37.5	1.61×10^{-15}	1.07×10^{-14}	1.23×10^{-14}	5.5	7.2	10.6	0.29	SHF
J160355.2+432836	16:03:55.2	43:28:36.7	3.58	7.9	6.1	14.0	9.98×10^{-16}	2.70×10^{-15}	3.69×10^{-15}	3.1	1.6	3.6	-0.13	S
J160356.2+431317	16:03:56.2	43:13:17.9	1.05	34.3	10.3	44.6	4.15×10^{-15}	4.55×10^{-15}	8.70×10^{-15}	13.2	3.5	13.7	-0.54	SHF
J160356.5+431626	16:03:56.5	43:16:26.0	5.37	4.4	9.4	13.9	5.57×10^{-16}	4.17×10^{-15}	4.72×10^{-15}	1.7	2.6	3.6	0.36	S
J160356.7+432358	16:03:56.7	43:23:58.9	0.68	5.1	29.4	34.5	6.50×10^{-16}	1.29×10^{-14}	1.36×10^{-14}	2.4	12.7	14.1	0.70	SHF
J160356.9+430734	16:03:56.9	43:07:34.0	2.44	2.9	8.8	11.7	3.55×10^{-16}	3.88×10^{-15}	4.23×10^{-15}	1.1	3.0	3.5	0.50	F
J160356.9+430950	16:03:56.9	43:09:50.9	1.54	4.1	8.1	12.1	4.91×10^{-16}	3.56×10^{-15}	4.05×10^{-15}	1.8	3.0	4.3	0.33	F
J160357.5+432349	16:03:57.5	43:23:49.8	0.58	1.0	29.1	30.1	1.30×10^{-16}	1.28×10^{-14}	1.30×10^{-14}	0.5	12.3	12.6	0.93	HF
J160358.4+430513	16:03:58.4	43:05:13.2	1.02	61.0	37.6	98.6	7.39×10^{-15}	1.65×10^{-14}	2.39×10^{-14}	20.4	11.8	26.4	-0.24	SHF
J160358.7+431553	16:03:58.7	43:15:53.6	2.20	32.1	7.6	39.7	4.06×10^{-15}	3.34×10^{-15}	7.39×10^{-15}	11.3	1.9	9.2	-0.62	SF
J160359.8+431934	16:03:59.8	43:19:34.6	1.46	6.8	1.5	8.3	8.63×10^{-16}	6.41×10^{-16}	1.50×10^{-15}	3.3	0.6	3.3	-0.65	SF
J160359.9+431142	16:03:59.9	43:11:42.7	1.03	2.1	19.6	21.6	2.48×10^{-16}	8.62×10^{-15}	8.87×10^{-15}	0.9	7.4	7.7	0.81	HF
J160400.1+432231	16:04:00.1	43:22:31.3	0.60	18.4	8.9	27.3	2.32×10^{-15}	3.93×10^{-15}	6.25×10^{-15}	9.1	4.0	12.4	-0.35	SF
J160400.2+430947	16:04:00.2	43:09:47.9	1.00	14.0	8.5	22.5	1.70×10^{-15}	3.73×10^{-15}	5.43×10^{-15}	6.2	3.2	8.1	-0.25	SHF
J160400.5+431706	16:04:00.5	43:17:06.2	2.01	20.5	21.3	41.8	2.48×10^{-15}	9.37×10^{-15}	1.19×10^{-14}	6.8	5.3	9.4	0.02	SHF
J160401.0+431153	16:04:01.0	43:11:53.0	1.32	0.7	11.6	12.3	7.94×10^{-17}	5.10×10^{-15}	5.18×10^{-15}	0.3	4.3	4.2	0.89	HF
J160401.3+431351	16:04:01.3	43:13:51.2	0.88	36.2	18.9	55.2	4.39×10^{-15}	8.32×10^{-15}	1.27×10^{-14}	15.4	6.7	18.6	-0.31	SHF
J160402.1+431333	16:04:02.1	43:13:33.6	0.96	9.5	33.1	42.7	1.16×10^{-15}	1.46×10^{-14}	1.57×10^{-14}	4.6	12.4	15.6	0.55	SHF
J160403.7+431136	16:04:03.7	43:11:36.5	2.17	6.2	4.8	11.0	7.49×10^{-16}	2.13×10^{-15}	2.88×10^{-15}	2.9	2.0	4.3	-0.12	SHF
J160404.3+431013	16:04:04.3	43:10:13.8	0.81	13.7	6.2	19.9	1.66×10^{-15}	2.74×10^{-15}	4.40×10^{-15}	6.3	2.7	8.3	-0.37	SF
J160404.6+432906	16:04:04.6	43:29:06.3	2.58	7.5	9.4	17.0	9.51×10^{-16}	4.16×10^{-15}	5.11×10^{-15}	2.7	2.6	4.2	0.11	F
J160405.1+431519	16:04:05.1	43:15:19.4	2.36	10.5	3.5	14.0	1.27×10^{-15}	1.56×10^{-15}	2.83×10^{-15}	4.0	1.2	4.2	-0.50	SF
J160405.1+430654	16:04:05.1	43:06:54.4	2.23	7.7	5.3	13.0	9.34×10^{-16}	2.34×10^{-15}	3.27×10^{-15}	3.3	2.0	4.6	-0.18	SF
J160405.3+432110	16:04:05.3	43:21:10.7	0.48	21.7	20.4	42.1	2.75×10^{-15}	9.00×10^{-15}	1.17×10^{-14}	10.7	8.4	17.5	-0.03	SHF
J160405.4+431121	16:04:05.4	43:11:22.0	1.38	4.1	7.2	11.3	5.00×10^{-16}	3.18×10^{-15}	3.68×10^{-15}	2.0	3.0	4.7	0.27	SHF
J160405.6+432351	16:04:05.6	43:23:51.6	0.47	33.9	26.1	60.0	4.29×10^{-15}	1.15×10^{-14}	1.58×10^{-14}	17.3	10.7	25.5	-0.13	SHF

Table 3
(Continued)

Source Name	R.A. (J2000)	Decl. (J2000)	Error ($''$)	(Soft)	Net Cnts ^a (Hard)	(Full)	(Soft)	F_x^b (Hard)	(Full)	(Soft)	Sig ^c (Hard)	(Full)	HR	Wavdetect ^d Flag
J160405.9+433128	16:04:05.9	43:31:28.6	3.90	11.0	11.9	22.9	1.39×10^{-15}	5.23×10^{-15}	6.63×10^{-15}	2.9	2.2	3.8	0.04	F
J160406.0+431807	16:04:06.0	43:18:07.6	0.83	32.2	15.3	47.5	4.08×10^{-15}	6.74×10^{-15}	1.08×10^{-14}	13.8	5.7	16.7	-0.36	SHF
J160406.1+430532	16:04:06.1	43:05:32.8	1.56	8.3	19.3	27.6	1.00×10^{-15}	8.51×10^{-15}	9.51×10^{-15}	3.6	7.0	9.3	0.40	HF
J160406.3+432125	16:04:06.3	43:21:25.8	0.22	98.1	47.1	145.2	1.24×10^{-14}	2.08×10^{-14}	3.32×10^{-14}	47.8	19.1	59.4	-0.35	SHF
J160406.6+430545	16:04:06.6	43:05:45.3	1.40	24.9	8.4	33.4	3.02×10^{-15}	3.72×10^{-15}	6.74×10^{-15}	10.9	2.9	11.1	-0.49	SHF
J160407.0+431445	16:04:07.0	43:14:45.8	0.82	44.5	19.4	63.9	5.40×10^{-15}	8.53×10^{-15}	1.39×10^{-14}	18.4	6.6	20.7	-0.39	SHF
J160407.5+432639	16:04:07.5	43:26:40.0	0.49	72.4	37.4	109.7	9.15×10^{-15}	1.65×10^{-14}	2.56×10^{-14}	32.1	14.9	41.7	-0.32	SHF
J160407.7+431712	16:04:07.7	43:17:12.7	1.85	26.0	20.6	46.6	3.15×10^{-15}	9.05×10^{-15}	1.22×10^{-14}	8.9	4.9	10.3	-0.12	SHF
J160408.0+431736	16:04:08.0	43:17:36.4	2.46	14.4	18.4	32.9	1.75×10^{-15}	8.12×10^{-15}	9.86×10^{-15}	4.7	4.4	7.1	0.12	SHF
J160408.9+431455	16:04:08.9	43:14:56.0	0.41	123.0	75.7	198.8	1.49×10^{-14}	3.33×10^{-14}	4.82×10^{-14}	51.7	23.8	60.2	-0.24	SHF
J160408.9+431825	16:04:08.9	43:18:25.8	1.51	2.8	12.7	15.4	3.51×10^{-16}	5.58×10^{-15}	5.93×10^{-15}	1.2	4.8	5.4	0.64	HF
J160409.0+431307	16:04:09.0	43:13:07.1	1.64	5.5	3.5	9.1	6.72×10^{-16}	1.56×10^{-15}	2.23×10^{-15}	2.8	1.4	3.7	-0.22	SF
J160409.4+430344	16:04:09.4	43:03:44.9	3.19	10.9	1.7	12.6	1.32×10^{-15}	7.39×10^{-16}	2.06×10^{-15}	4.1	0.4	3.2	-0.73	SF
J160409.7+432341	16:04:09.7	43:23:41.3	0.88	3.4	4.8	8.1	4.26×10^{-16}	2.10×10^{-15}	2.53×10^{-15}	1.6	2.1	3.5	0.17	F
J160410.0+430437	16:04:10.0	43:04:37.2	0.98	90.3	25.2	115.5	1.09×10^{-14}	1.11×10^{-14}	2.20×10^{-14}	37.5	7.7	34.4	-0.56	SHF
J160410.2+432614	16:04:10.2	43:26:14.6	0.46	77.2	23.7	100.8	9.76×10^{-15}	1.04×10^{-14}	2.02×10^{-14}	37.9	9.4	40.9	-0.53	SHF
J160410.9+432111	16:04:10.9	43:21:11.0	0.87	2.5	7.9	10.3	3.12×10^{-16}	3.48×10^{-15}	3.79×10^{-15}	1.2	3.2	4.2	0.52	F
J160411.4+432733	16:04:11.4	43:27:33.5	2.17	9.2	5.7	14.9	1.16×10^{-15}	2.52×10^{-15}	3.69×10^{-15}	3.9	2.1	5.1	-0.23	SF
J160411.5+430148	16:04:11.5	43:01:48.2	2.14	69.1	4.5	73.5	8.37×10^{-15}	1.96×10^{-15}	1.03×10^{-14}	20.1	1.0	14.6	-0.88	SF
J160412.6+431002	16:04:12.6	43:10:02.1	1.61	4.2	2.5	6.6	5.05×10^{-16}	1.08×10^{-15}	1.59×10^{-15}	2.1	1.1	3.1	-0.26	F
J160412.8+432627	16:04:12.8	43:26:27.8	0.76	31.3	9.1	40.4	3.95×10^{-15}	4.01×10^{-15}	7.96×10^{-15}	14.1	3.5	15.2	-0.55	SHF
J160413.1+430927	16:04:13.1	43:09:27.6	1.32	7.7	0.0	7.7	9.30×10^{-16}	0.00	9.30×10^{-16}	3.8	0.0	3.4	-1.00	S
J160413.8+432757	16:04:13.8	43:27:58.0	2.72	7.0	0.9	7.9	8.86×10^{-16}	3.77×10^{-16}	1.26×10^{-15}	3.2	0.3	2.7	-0.78	SF
J160415.5+431016	16:04:15.5	43:10:16.6	0.37	53.0	25.4	78.4	6.42×10^{-15}	1.12×10^{-14}	1.76×10^{-14}	25.2	10.2	31.2	-0.35	SHF
J160415.6+431410	16:04:15.6	43:14:10.5	1.16	5.3	11.6	16.8	6.39×10^{-16}	5.09×10^{-15}	5.73×10^{-15}	2.4	4.4	6.1	0.37	HF
J160415.8+433120	16:04:15.8	43:31:20.8	6.93	16.5	3.1	19.6	2.09×10^{-15}	1.39×10^{-15}	3.47×10^{-15}	5.0	0.6	3.7	-0.68	S
J160416.2+431419	16:04:16.2	43:14:19.1	0.74	29.9	18.7	48.7	3.62×10^{-15}	8.25×10^{-15}	1.19×10^{-14}	14.0	7.3	18.7	-0.23	SHF
J160416.6+432440	16:04:16.6	43:24:40.5	1.14	5.3	4.2	9.5	6.73×10^{-16}	1.86×10^{-15}	2.53×10^{-15}	2.5	1.9	4.1	-0.12	F
J160417.5+433025	16:04:17.5	43:30:25.1	2.20	9.0	37.5	46.4	1.13×10^{-15}	1.65×10^{-14}	1.77×10^{-14}	3.0	8.5	9.7	0.61	HF
J160418.2+430018	16:04:18.2	43:00:18.3	9.42	9.6	9.1	18.7	1.16×10^{-15}	4.02×10^{-15}	5.19×10^{-15}	2.9	2.0	3.7	-0.02	S
J160418.2+431925	16:04:18.2	43:19:25.5	0.75	42.5	0.4	42.9	5.37×10^{-15}	1.77×10^{-16}	5.55×10^{-15}	20.5	0.2	17.2	-0.98	SF
J160419.0+430700	16:04:19.0	43:07:00.9	1.85	6.8	0.0	6.8	8.24×10^{-16}	0.00	8.24×10^{-16}	3.3	0.0	3.0	-1.00	S
J160419.1+431104	16:04:19.1	43:11:04.3	0.28	40.5	15.1	55.6	4.91×10^{-15}	6.64×10^{-15}	1.15×10^{-14}	19.8	6.4	23.7	-0.46	SHF

Table 3
(Continued)

Source Name	R.A. (J2000)	Decl. (J2000)	Error (")	(Soft)	Net Cnts ^a (Hard)	(Full)	(Soft)	F_x^b (Hard)	(Full)	(Soft)	Sig ^c (Hard)	(Full)	HR	Wavdetect ^d Flag
J160419.2+431600	16:04:19.2	43:16:00.5	2.91	13.0	2.9	15.9	1.65×10^{-15}	1.27×10^{-15}	2.92×10^{-15}	4.5	0.8	4.0	-0.64	SF
J160420.3+432651	16:04:20.3	43:26:51.4	2.21	6.7	0.8	7.5	8.44×10^{-16}	3.57×10^{-16}	1.20×10^{-15}	3.1	0.3	2.7	-0.78	SF
J160421.1+431521	16:04:21.1	43:15:21.4	2.27	10.0	1.7	11.6	1.21×10^{-15}	7.39×10^{-16}	1.95×10^{-15}	4.2	0.6	3.7	-0.71	SF
J160421.8+432354	16:04:21.8	43:23:54.7	0.18	382.3	246.5	628.8	4.83×10^{-14}	1.09×10^{-13}	1.57×10^{-13}	182.5	100.3	253.9	-0.22	SHF
J160421.9+432716	16:04:21.9	43:27:16.8	1.26	17.8	10.4	28.2	2.25×10^{-15}	4.58×10^{-15}	6.82×10^{-15}	7.8	3.6	9.4	-0.26	SHF
J160423.5+431249	16:04:23.5	43:12:49.4	0.72	11.0	11.9	22.9	1.33×10^{-15}	5.24×10^{-15}	6.57×10^{-15}	5.5	4.9	9.5	0.04	SHF
J160423.9+431125	16:04:23.9	43:11:25.9	0.29	48.5	19.6	68.1	5.87×10^{-15}	8.63×10^{-15}	1.45×10^{-14}	23.2	8.0	27.8	-0.42	SHF
J160423.9+431610	16:04:23.9	43:16:10.3	1.23	41.7	12.3	54.0	5.06×10^{-15}	5.41×10^{-15}	1.05×10^{-14}	14.8	3.7	14.8	-0.54	SHF
J160424.1+431106	16:04:24.1	43:11:06.2	0.73	7.4	1.8	9.3	9.02×10^{-16}	8.05×10^{-16}	1.71×10^{-15}	3.6	0.8	4.0	-0.61	SF
J160424.2+433421	16:04:24.2	43:34:21.1	16.68	26.1	15.7	41.7	3.29×10^{-15}	6.91×10^{-15}	1.02×10^{-14}	5.7	2.7	6.1	-0.25	S
J160424.7+432208	16:04:24.7	43:22:08.8	1.13	6.7	1.8	8.4	8.43×10^{-16}	7.80×10^{-16}	1.62×10^{-15}	3.1	0.7	3.4	-0.58	SF
J160425.2+430133	16:04:25.2	43:01:33.5	4.22	11.6	8.4	20.0	1.40×10^{-15}	3.70×10^{-15}	5.10×10^{-15}	3.3	1.8	3.8	-0.16	SF
J160425.9+431245	16:04:25.9	43:12:45.2	0.69	18.4	7.5	25.9	2.23×10^{-15}	3.31×10^{-15}	5.54×10^{-15}	8.3	3.2	10.4	-0.42	SHF
J160426.1+430754	16:04:26.1	43:07:55.0	1.01	10.6	6.3	16.9	1.28×10^{-15}	2.78×10^{-15}	4.06×10^{-15}	5.0	2.7	7.0	-0.25	SHF
J160426.3+431742	16:04:26.3	43:17:42.3	2.84	5.5	9.5	14.9	6.91×10^{-16}	4.17×10^{-15}	4.87×10^{-15}	2.2	3.2	4.6	0.27	F
J160426.4+432634	16:04:26.4	43:26:34.8	1.78	8.7	3.6	12.3	1.10×10^{-15}	1.59×10^{-15}	2.69×10^{-15}	3.9	1.4	4.5	-0.41	SF
J160427.5+432252	16:04:27.5	43:22:52.5	1.10	3.2	8.6	11.8	4.07×10^{-16}	3.80×10^{-15}	4.20×10^{-15}	1.6	3.4	4.6	0.46	HF
J160428.3+430940	16:04:28.3	43:09:40.8	1.41	5.0	4.3	9.3	6.00×10^{-16}	1.90×10^{-15}	2.50×10^{-15}	2.5	1.8	3.9	-0.07	SF
J160429.1+432830	16:04:29.1	43:28:30.1	2.58	17.4	6.9	24.3	2.20×10^{-15}	3.04×10^{-15}	5.23×10^{-15}	6.2	1.8	6.0	-0.43	SF
J160429.5+432306	16:04:29.5	43:23:06.8	1.01	8.7	8.2	16.9	1.10×10^{-15}	3.62×10^{-15}	4.72×10^{-15}	4.1	3.0	6.2	-0.03	SHF
J160430.7+430623	16:04:30.7	43:06:23.1	2.03	7.5	0.0	7.5	9.10×10^{-16}	0.00	9.10×10^{-16}	3.4	0.0	2.7	-1.00	SF
J160431.4+432954	16:04:31.4	43:29:54.7	2.10	34.5	28.1	62.6	4.36×10^{-15}	1.24×10^{-14}	1.68×10^{-14}	10.4	6.2	12.4	-0.10	SHF
J160432.2+430401	16:04:32.2	43:04:01.9	3.39	9.0	9.6	18.6	1.09×10^{-15}	4.23×10^{-15}	5.32×10^{-15}	3.4	2.7	4.9	0.03	SF
J160432.7+430802	16:04:32.7	43:08:02.4	0.26	159.7	63.9	223.6	1.93×10^{-14}	2.81×10^{-14}	4.75×10^{-14}	78.1	25.6	91.0	-0.43	SHF
J160433.3+430339	16:04:33.3	43:03:39.4	0.94	172.3	29.0	201.3	2.09×10^{-14}	1.27×10^{-14}	3.36×10^{-14}	67.7	8.0	53.6	-0.71	SHF
J160433.8+431833	16:04:33.8	43:18:33.0	0.45	206.2	72.1	278.3	2.61×10^{-14}	3.18×10^{-14}	5.79×10^{-14}	77.3	21.3	76.5	-0.48	SHF
J160433.8+432352	16:04:33.8	43:23:52.4	1.31	4.0	13.1	17.1	5.10×10^{-16}	5.78×10^{-15}	6.29×10^{-15}	1.8	4.7	5.8	0.53	SHF
J160435.5+432112	16:04:35.5	43:21:12.3	1.42	12.9	7.6	20.5	1.63×10^{-15}	3.36×10^{-15}	4.99×10^{-15}	5.4	2.7	6.8	-0.26	SF
J160435.8+430551	16:04:35.8	43:05:51.8	3.73	9.3	3.2	12.5	1.12×10^{-15}	1.43×10^{-15}	2.55×10^{-15}	3.8	1.2	4.3	-0.48	S
J160436.0+431929	16:04:36.0	43:19:29.3	0.84	33.0	50.9	83.9	4.18×10^{-15}	2.24×10^{-14}	2.66×10^{-14}	13.0	16.9	25.4	0.21	SHF
J160436.4+431808	16:04:36.4	43:18:08.4	3.33	11.4	0.0	11.4	1.44×10^{-15}	0.00	1.44×10^{-15}	4.3	0.0	3.0	-1.00	SF
J160436.7+432141	16:04:36.7	43:21:41.4	1.17	16.4	13.5	29.9	2.07×10^{-15}	5.94×10^{-15}	8.02×10^{-15}	6.4	4.9	9.6	-0.10	SHF
J160437.5+432010	16:04:37.5	43:20:10.2	1.83	13.4	2.9	16.3	1.69×10^{-15}	1.29×10^{-15}	2.99×10^{-15}	5.3	1.0	5.2	-0.64	SF

Table 3
(Continued)

Source Name	R.A. (J2000)	Decl. (J2000)	Error (")	(Soft)	Net Cnts ^a (Hard)	(Full)	(Soft)	F_x^b (Hard)	(Full)	(Soft)	Sig ^c (Hard)	(Full)	HR	Wavdetect ^d Flag
J160437.9+430753	16:04:37.9	43:07:53.0	0.73	38.3	14.2	52.5	4.64×10^{-15}	6.25×10^{-15}	1.09×10^{-14}	16.8	5.3	18.9	-0.46	SHF
J160438.3+432625	16:04:38.3	43:26:25.2	1.64	18.7	49.4	68.1	2.36×10^{-15}	2.18×10^{-14}	2.42×10^{-14}	7.7	14.8	19.2	0.45	SHF
J160438.4+430729	16:04:38.4	43:07:29.1	0.47	87.2	57.4	144.6	1.06×10^{-14}	2.53×10^{-14}	3.58×10^{-14}	40.2	20.3	50.6	-0.21	SHF
J160439.3+432419	16:04:39.3	43:24:19.6	1.47	11.1	14.2	25.2	1.40×10^{-15}	6.24×10^{-15}	7.64×10^{-15}	4.7	4.8	8.1	0.12	SF
J160439.5+430509	16:04:39.5	43:05:09.8	2.69	8.3	6.0	14.3	1.01×10^{-15}	2.63×10^{-15}	3.64×10^{-15}	3.4	1.9	4.2	-0.16	SF
J160441.7+432057	16:04:41.7	43:20:57.8	1.45	16.0	17.5	33.5	2.02×10^{-15}	7.72×10^{-15}	9.74×10^{-15}	6.3	5.4	9.6	0.04	SHF
J160443.3+431348	16:04:43.3	43:13:48.2	0.75	106.3	33.2	139.5	1.29×10^{-14}	1.46×10^{-14}	2.75×10^{-14}	42.5	10.3	41.1	-0.52	SHF
J160444.6+432026	16:04:44.6	43:20:26.8	0.98	68.3	36.3	104.6	8.63×10^{-15}	1.60×10^{-14}	2.46×10^{-14}	22.9	10.1	26.0	-0.31	SHF
J160446.0+432234	16:04:46.0	43:22:34.5	0.54	164.4	65.7	230.2	2.08×10^{-14}	2.90×10^{-14}	4.98×10^{-14}	61.0	18.1	59.6	-0.43	SHF
J160447.5+431723	16:04:47.5	43:17:23.9	11.85	8.7	23.7	32.4	1.05×10^{-15}	1.04×10^{-14}	1.15×10^{-14}	2.9	5.6	7.0	0.46	H
J160448.4+430807	16:04:48.4	43:08:07.3	1.17	34.2	14.1	48.3	4.14×10^{-15}	6.20×10^{-15}	1.03×10^{-14}	13.0	4.0	12.9	-0.42	SHF
J160449.5+430723	16:04:49.5	43:07:23.4	3.02	0.0	14.7	14.7	0.00	6.48×10^{-15}	6.48×10^{-15}	0.0	4.6	4.0	1.00	HF
J160450.2+432158	16:04:50.2	43:21:58.3	0.95	164.3	73.7	237.9	2.08×10^{-14}	3.25×10^{-14}	5.33×10^{-14}	53.2	18.4	54.0	-0.38	SHF
J160451.3+431548	16:04:51.3	43:15:48.8	1.52	104.5	47.8	152.3	1.27×10^{-14}	2.10×10^{-14}	3.37×10^{-14}	33.9	11.4	33.4	-0.37	SHF
J160453.3+431912	16:04:53.3	43:19:12.2	2.65	26.7	14.0	40.8	3.38×10^{-15}	6.19×10^{-15}	9.57×10^{-15}	7.5	2.9	7.6	-0.31	SF
J160454.3+431036	16:04:54.3	43:10:36.5	2.43	7.2	7.1	14.3	8.71×10^{-16}	3.11×10^{-15}	3.98×10^{-15}	2.6	1.9	3.6	-0.01	F
J160454.3+430829	16:04:54.3	43:08:29.1	3.84	9.0	0.0	9.0	1.09×10^{-15}	0.00	1.09×10^{-15}	3.3	0.0	2.4	-1.00	SF
J160454.7+431013	16:04:54.7	43:10:13.7	5.14	12.1	0.0	12.1	1.47×10^{-15}	0.00	1.47×10^{-15}	4.4	0.0	3.1	-1.00	S
J160455.5+431445	16:04:55.5	43:14:45.3	4.18	50.9	17.7	68.5	6.16×10^{-15}	7.77×10^{-15}	1.39×10^{-14}	18.8	4.6	17.1	-0.48	SF
J160456.9+432037	16:04:56.9	43:20:37.2	3.50	16.5	8.6	25.1	2.09×10^{-15}	3.79×10^{-15}	5.88×10^{-15}	4.8	1.8	4.7	-0.31	SF
J160459.6+430508	16:04:59.6	43:05:08.2	5.19	16.1	17.1	33.1	1.95×10^{-15}	7.51×10^{-15}	9.46×10^{-15}	4.7	3.4	6.0	0.03	F
J160459.8+431957	16:04:59.8	43:19:57.3	2.51	54.2	31.2	85.5	6.86×10^{-15}	1.38×10^{-14}	2.06×10^{-14}	14.3	5.5	13.9	-0.27	SHF
J160500.3+431028	16:05:00.3	43:10:28.0	1.72	41.7	25.4	67.1	5.05×10^{-15}	1.12×10^{-14}	1.62×10^{-14}	11.9	5.7	13.4	-0.24	SHF
J160501.1+430724	16:05:01.1	43:07:24.1	2.84	10.5	22.5	33.0	1.27×10^{-15}	9.90×10^{-15}	1.12×10^{-14}	3.2	5.0	6.5	0.36	HF
J160501.9+430914	16:05:01.9	43:09:14.5	2.54	13.2	15.6	28.8	1.60×10^{-15}	6.86×10^{-15}	8.46×10^{-15}	4.0	3.6	5.9	0.08	SF
J160502.9+430602	16:05:02.9	43:06:02.8	6.68	9.4	9.3	18.7	1.14×10^{-15}	4.07×10^{-15}	5.22×10^{-15}	2.4	2.0	3.4	-0.01	S
J160503.0+432144	16:05:03.0	43:21:44.0	0.93	269.6	308.9	578.6	3.41×10^{-14}	1.36×10^{-13}	1.70×10^{-13}	73.3	60.7	101.3	0.07	SHF
J160505.1+430632	16:05:05.1	43:06:32.5	6.70	7.6	10.1	17.7	9.19×10^{-16}	4.44×10^{-15}	5.36×10^{-15}	2.0	2.0	3.1	0.14	S
J160506.5+431032	16:05:06.5	43:10:32.7	5.72	11.1	11.4	22.5	1.34×10^{-15}	5.04×10^{-15}	6.38×10^{-15}	3.5	2.6	4.6	0.02	S

Notes.

^a Net Cnts: aperture corrected net counts.

^b In units of $\text{erg cm}^{-2} \text{s}^{-1}$.

^c Detection significance as determined by aperture photometry.

^d Band in which source detected using `wavdetect`; soft = 0.5–2 keV, hard = 2–8 keV, full = 0.5–8 keV.

(This table is also available in a machine-readable form in the online journal.)

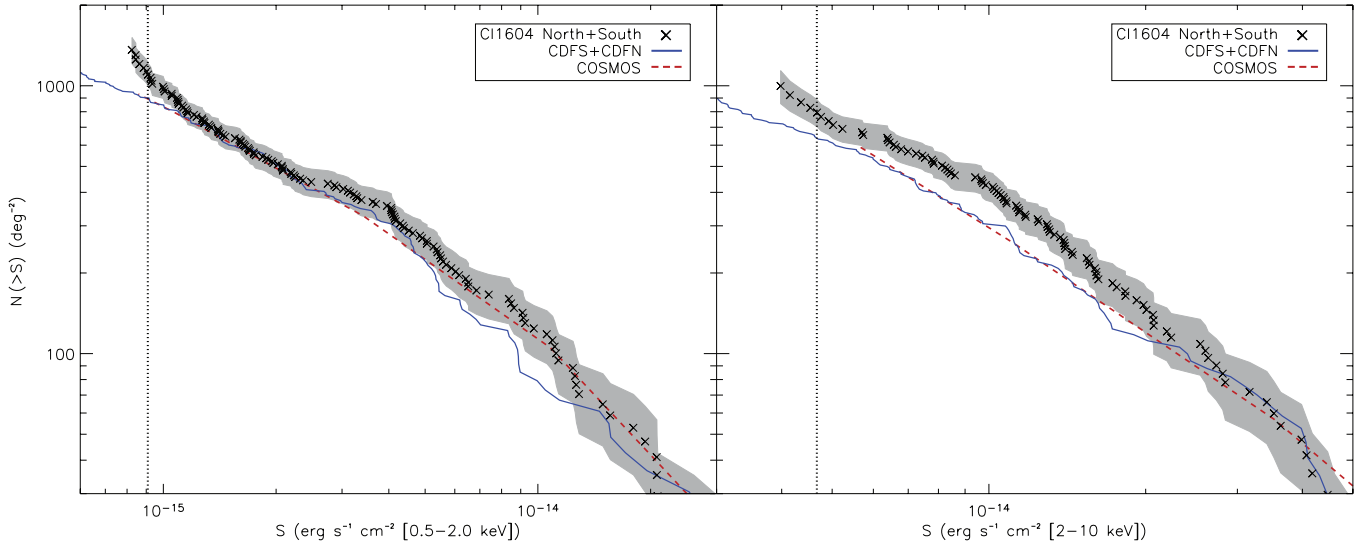


Figure 4. Combined cumulative source number counts vs. flux for the northern and southern pointings of the Cl1604 supercluster in the soft (0.5–2 keV; left) and hard bands (2–10 keV; right). The shaded region denotes a 1σ variance in the number counts. Only sources detected above the 3σ level are included. The results of an *XMM-Newton* survey of the COSMOS field (Cappelluti et al. 2007) and that of a 130 ks *Chandra* observation of the CDFS and CDFN are shown for comparison (the dashed and solid lines, respectively). The vertical dotted line represents the flux at which our sky coverage dropped to 20% of the full ACIS-I FOV.

off-axis angle. In order to calculate Ω_i , we constructed a flux limit map using a similar method to that employed by Johnson et al. (2003) and Cappelluti et al. (2005). First, all point sources detected by *wavdetect* (at all significance levels) in our two pointings were replaced with an estimate of the local background with the CIAO tool *dmfilth*. These images were then binned to a pixel scale of $32'' \text{ pixel}^{-1}$ to produce a coarse background map. Given Equation (1), the flux limit, S_{lim} , for a 3σ point-source detection in any one pixel is then

$$S_{\text{lim}} = \frac{3Vk}{t} \left(1.0 + \sqrt{0.75 + B\pi R_{95}^2 / A_{\text{pix}}} \right), \quad (4)$$

where B is the background level in counts, A_{pix} is the sky area covered by one binned pixel, R_{95} is the aforementioned 95% enclosed energy radius used for our aperture photometry, V is a vignetting correction factor, k is the count rate to flux conversion factor, and t is the exposure time at the aim point of the observation. The values for R_{95} are determined for each pixel given its off-axis angle, while V is estimated by normalizing an exposure map to its maximum value at the aim point of the observation. Using this flux limit map, we can calculate Ω_i by summing the sky area covered by all pixels with S_{lim} equal to or greater than the flux of the i th source. An important point to note is that we have not removed or masked any diffuse cluster emission and have instead treated it as an enhanced local background in constructing the flux limit map. This allows us to properly account for the fact that our flux limit for point-source detection is effectively increased in the presence of diffuse emission when we calculate the $1/\Omega_i$ corrective weights.

The combined cumulative source number counts for the northern and southern pointings of the Cl1604 supercluster are shown in Figure 4. The distribution is shown in the 0.5–2 keV (left panel) and 2–10 keV (right panel) bands. The latter was chosen to ease comparison with previous studies and was obtained by extrapolating our 2–8 keV fluxes to 10 keV; we refer to 2–10 keV band as the hard_{10} band hereafter. Also shown are the cumulative number counts measured in the COSMOS field (Scoville et al. 2007) and the combined counts obtained in

the *Chandra* Deep Field South and North (CDFS and CDFN; Rosati et al. 2002; Brandt et al. 2001). The COSMOS results are those of Cappelluti et al. (2007) converted to a spectral index of $\gamma = 1.4$, while the combined CDFS and CDFN counts are the result of our own re-analysis of two single pointings in each field. Data for these fields were obtained from the *Chandra* archive⁶ and analyzed in an identical manner to that of the Cl1604 field. The two pointings used have observation ID numbers of 581 and 2232; each is a single pointing of the ACIS-I array with exposure times of roughly 130 ks. We have combined the number counts obtained for each field separately into a unified reference field (hereafter CDF) to which we compare our source counts throughout. It is important to note that we have decided not to use any portion of our data to estimate the blank-field number counts as the supercluster extends over much of the FOV of our observations (clusters and/or galaxy overdensities fall on six of the eight ACIS chips). Therefore, despite the fact that the COSMOS field was analyzed by a different group and the CDF fields observed at different epochs than our observations we must rely on these data sets to provide blank reference fields for comparison.

In the soft band, we find that the number of sources detected in the Cl1604 pointing and the composite blank field are statistically consistent ($<1\sigma$ difference) over a majority of the sampled flux range. The greatest deviation of the Cl1604 counts is observed at $9.1 \times 10^{-15} \text{ erg s}^{-1} \text{ cm}^{-2}$, where we find a 2.0σ excess in the supercluster field relative to the CDF counts. This is likely due to the underdensity of soft sources previously reported at these fluxes in the CDFS (Yang et al. 2003) which suppresses the combined CDF number counts at this flux. When our measured source density is compared with that of the COSMOS field, which covers a significantly larger area than the CDFS, we find excellent agreement at the bright end of the distribution. We also observe a deviation from both the CDF and COSMOS fields near our 3σ flux limit, but we caution that at these fluxes the source counts are heavily weighted due to a rapidly

⁶ <http://cxc.harvard.edu/>

decreasing sky coverage. At a flux of $9.1 \times 10^{-16} \text{ erg s}^{-1} \text{ cm}^{-2}$, the effective detector area drops to 20% of the total ACIS-I FOV. As is common in the literature, we adopt this flux as our effective minimum for this analysis; the flux is denoted by a vertical dotted line in Figure 4.

Unlike the general agreement found between the supercluster and blank-field counts in the soft band, we find that the source density in the hard₁₀ band significantly surpasses the density measured in both the reference and COSMOS fields. As a result of a steeper power-law slope, the C11604 counts deviate from the blank-field distribution near 2×10^{-14} and reach a maximum excess at $9.7 \times 10^{-15} \text{ erg s}^{-1} \text{ cm}^{-2}$, where we find a 2.5σ overdensity relative to the CDF counts. Below this flux a break in the source counts is observed and the slope of the distribution flattens, reducing the difference between the supercluster and blank-field counts. At our 20% FOV flux limit of $4.7 \times 10^{-15} \text{ erg s}^{-1} \text{ cm}^{-2}$, the excess is reduced to a 1.7σ deviation.

To parameterize our cumulative flux distribution, we have fitted the unbinned soft- and hard₁₀-band counts in the C11604 field with a power-law model of the form

$$N(<S) = k \left(\frac{S}{S_0} \right)^{-\alpha} \text{ (deg}^{-2}\text{)} \quad (5)$$

using the maximum likelihood method described by Crawford et al. (1970) and Murdoch et al. (1973). Although a single power-law model is not an ideal parameterization of the number counts in the soft band, it does provide an adequate fit in the hard band above the break in the distribution. The normalization of the model, k , was determined by requiring that the best-fit slope, α , reproduces the number of sources observed at the flux limit. Our best-fit single power-law model in the soft band is

$$N_{0.52}(<S) = 550 \left(\frac{S}{2 \times 10^{-15}} \right)^{-0.88 \pm 0.08}.$$

In the hard₁₀ band there is a clear break at $9.2 \times 10^{-15} \text{ erg s}^{-1} \text{ cm}^{-2}$, below which the slope of the distribution flattens, in qualitative agreement with previous deep *Chandra* and *XMM-Newton* surveys (Brandt & Hasinger 2005). Performing a maximum likelihood fit to the bright-end counts above the break, we obtain a power-law model of

$$N_{210}(<S) = 419 \left(\frac{S}{1 \times 10^{-14}} \right)^{-1.59 \pm 0.21}.$$

Our best-fit slope of $\alpha = 1.59 \pm 0.21$ over the flux range of 1×10^{-14} to $4 \times 10^{-14} \text{ erg s}^{-1} \text{ cm}^{-2}$ is significantly steeper than the slopes found over similar fluxes in the CDFN (1.0 ± 0.3 ; Brandt et al. 2001) and the CDFS (0.61 ± 0.1 ; Rosati et al. 2002). This difference in the slope of the cumulative distribution is responsible for building up the 2.5σ source excess observed at $\sim 1 \times 10^{-14} \text{ erg s}^{-1} \text{ cm}^{-2}$.

It appears that over the FOV of nearly two full ACIS-I pointings covering the C11604 supercluster we find no significant excess of soft X-ray sources relative to a blank field, but a clear overdensity of harder, presumably more obscured sources is detected. Cappelluti et al. (2005) previously reported a correlation between the amplitude of the overdensity observed in the hard₁₀ band and cluster redshift. Normalizing our observed source density to the mean amplitude of their reference field counts at $1 \times 10^{-14} \text{ erg s}^{-1} \text{ cm}^{-2}$, we find that the C11604 field

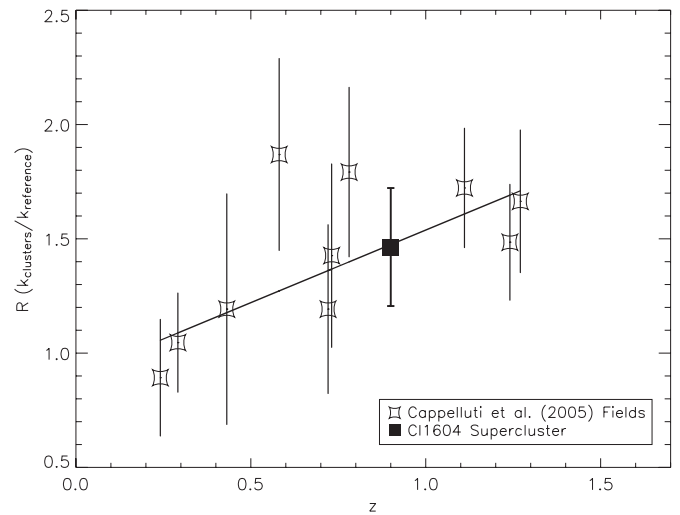


Figure 5. Overdensity amplitude as a function of cluster redshift observed by Cappelluti et al. (2005) in the field of 10 clusters in the hard₁₀ band. Overplotted is the overdensity we measure in the field of the C11604 supercluster. We find that the C11604 counts are in excellent agreement with their best-fit linear relation. (Adapted from Figure 6 of Cappelluti et al. 2005.)

exhibits a factor of 1.47 overdensity of hard₁₀-band sources. In Figure 5, we plot the overdensity amplitude as a function of cluster redshift observed by Cappelluti et al. (2005) along with the overdensity amplitude in the C11604 field. We find that the C11604 counts are in excellent agreement with their best-fit linear relation.

It has also been noted that the observed field-to-field variation in the hard band is substantially above the level expected due to Poisson noise (Cowie et al. 2002), suggesting that the variations are due to intrinsic clustering of the population and their tracing of underlying large-scale structures. If the excess sources that we have detected are associated with the C11604 supercluster then this observation, along with the fact that we do not see such an overdensity in the soft band, seems to support the notion that more obscured, harder X-ray sources are more highly biased tracers of LSS than their softer counterparts. This issue has been debated with Yang et al. (2003) and Basilakos et al. (2004) finding an increased angular clustering amplitude of hard-band sources while Gilli et al. (2005) and Yang et al. (2006) find no dependence of the clustering scale length with X-ray spectral shape (see also Miyaji et al. 2007).

Finally, it is important to stress two points regarding the nature of the observed overdensity. First, if the excess sources are at the supercluster redshift of $z = 0.9$, then their luminosities strongly suggest that the sources are AGNs as opposed to powerful starburst galaxies. For example, a source detected at our 3σ flux limit would have a rest-frame 0.5–8 keV luminosity of $8.5 \times 10^{42} h_{70}^{-2} \text{ erg s}^{-1}$, far above the luminosity attributable to starburst galaxies (e.g., Bauer et al. 2002), making it highly unlikely that the source overdensity is due to increased starburst activity in the supercluster. Secondly, we point out that the observed overdensity persists over nearly two full ACIS-I pointings. The previously reported source overdensities have often been presented on a chip-by-chip basis ($8' \times 8'$; e.g., D'Elia et al. 2004; Cappelluti et al. 2005). On such scales Poisson noise may contribute a significant signal to fluctuations observed in the source counts (Cappelluti et al. 2007). In fact, Cappelluti et al. (2005) note that their observed excesses disappear when their source counts are integrated over an entire ACIS-I FOV. This is in agreement with Kim et al. (2004b) who find no

statistically significant difference between cluster and cluster-free fields on scales of $16' \times 16'$. The fact that our larger FOV has not smoothed away our observed overdensity suggests that the increased amplitude is not due to a statistical fluctuation, but instead due to sources which are indeed associated with the supercluster, whose constituent clusters extend over the entire FOV of the two pointings. In Section 3.4, we bolster this claim with evidence for a peak in the redshift distribution of X-ray sources near that of the C11604 system.

3.3. Matching to Optical Sources

To determine the origin of the overdensity observed in the number counts and to ascertain whether the sources are truly associated with the C11604 supercluster we searched for optical counterparts to all 161 unique point sources detected in the field of C11604 above the 3σ level in at least one of the three X-ray bands. Matching of our X-ray source list to the LFC + ACS optical catalog was carried out using the maximum likelihood technique described by Sutherland & Saunders (1992) and more recently implemented by Taylor et al. (2005) and Gilmour et al. (2007). The method gauges the likelihood that a given optical object is matched to an X-ray source by comparing the probability of finding a genuine counterpart with the positional offset and magnitude of the optical candidate relative to that of finding a similar object by chance. The key statistic used is known as the likelihood ratio, $LR_{i,j}$, which specifies the likelihood that X-ray source j is associated with optical object i . If we assume a Gaussian form for the probability distribution of the X-ray positional errors, it can be defined as

$$LR_{i,j} = \frac{e^{-r_{i,j}^2/2\sigma_j^2}}{\sigma_j^2 n(< m_i)}, \quad (6)$$

where $r_{i,j}$ is the positional offset between the optical object i and X-ray source j , $n(< m_i)$ is the number density of optical objects brighter than object j in the F814W (i') band in the ACS (LFC) catalog, and σ_j is the positional error associated with the X-ray source j .

The advantage of this approach over a simple nearest neighbor match is that $LR_{i,j}$ takes into account the density of objects as faint as the optical counterpart as well as the distance between sources and the X-ray positional errors. This is vitally important when matching to a source list drawn from deep, high-resolution ACS imaging, which has an extremely high surface density of faint sources. Without consideration of magnitude an inordinate number of X-ray sources would be matched to optical objects near the detection limit of the catalog. Instead, when surface density is taken into account, brighter sources, which are rarer in the optical catalog, are given an increased likelihood of being a genuine counterpart to an X-ray source compared to fainter sources with the same positional offset.

We considered an optical source a candidate counterpart if it fell within the positional error of an X-ray source and calculated $LR_{i,j}$ for each candidate-X-ray pair. Since the *Chandra* PSF degrades with increased distance from the aim point of the observation, the positional uncertainty associated with each X-ray source depends on its off-axis angle. To account for this effect we have determined the errors on our X-ray positions using the empirically derived relations of Kim et al. (2007), who find that centroiding errors increase exponentially with off-axis angle and decrease as the source counts increase with a power-law form. To simplify the calculation of $LR_{i,j}$, we have assumed that any optical positional errors are negligible compared to the

larger X-ray uncertainties, which ranged from $0'.5$ on-axis to $12''.0$ at $12'.1$ off-axis for a source detected with 10 counts.⁷

To calculate $n(< m_i)$ for a given optical counterpart, we determined the magnitude distribution of sources in the same subset of the composite optical catalog from which the candidate source was drawn. If the source fell within the boundaries of the ACS mosaic, $n(< m_i)$ was determined from the density and magnitude distribution of ACS-detected objects. A similar procedure was used for sources only detected in the LFC imaging.

While $LR_{i,j}$ provides the likelihood that the X-ray source j is associated with the optical object i , the ratio itself does not provide an estimate of the reliability of a given match. This can be obtained by comparing the value of $LR_{i,j}$ for a particular match with the distribution of $LR_{i,j}$ values for chance matches. We determined the latter by randomizing the positions of each X-ray source 10,000 times and recording the distribution of $LR_{i,j}$ values for the resulting chance matches to optical sources. Again, this process was done separately for X-ray sources falling within and outside the ACS imaging. Following Gilmour et al. (2007), the reliability of a match was defined as the probability of not obtaining $LR_{i,j}$ randomly,

$$R_{i,j} = 1 - \frac{\Sigma N(LR_j > LR_{i,j})}{10000}, \quad (7)$$

where $N(LR_j > LR_{i,j})$ is the number of chance matches in our Monte Carlo simulation with likelihood ratios that exceeded $LR_{i,j}$. Here, $R_{i,j}$ is essentially the binomial probability that a given match with a specific value of $LR_{i,j}$ is a true association and not a chance match.

Given the relatively large X-ray positional uncertainties and the high source density in our ACS imaging, there are often several candidate counterparts to any given X-ray source and many of these can have high reliability estimates. Following Rutledge et al. (2000), we can use $R_{i,j}$ to determine which optical candidate is the genuine counterpart and the probability that there is instead no genuine counterpart. Since $R_{i,j}$ is the probability that a given match is a true association, the probability that the optical source i is the genuine counterpart to the X-ray source j is

$$P_{i,j} = \frac{R_{i,j} \prod_{k \neq i}^M (1 - R_{k,j})}{S}. \quad (8)$$

Here, M is the total number of optical candidates and S is a normalization factor defined below. $P_{i,j}$ is simply the product of the probability that the i th optical object is a true association ($R_{i,j}$) with the probabilities that the remaining optical candidates are not ($1 - R_{k \neq i,j}$). Likewise, the probability that there is no genuine counterpart given M candidates is

$$P_{\text{none},j} = \frac{\prod_{k=1}^M (1 - R_{k,j})}{S} \quad (9)$$

where S is a normalization factor that varies for each source to ensure that the probabilities $P_{i,j}$ and $P_{\text{none},j}$ sum to unity.

Following Gilmour et al. (2007), we consider an X-ray source with a single-candidate counterpart to be matched to a given optical object if $P_{i,j} > 0.8$ for objects in the ACS catalog (i.e., the probability for a genuine match is four times that of

⁷ The quoted errors are at the 95% confidence level.

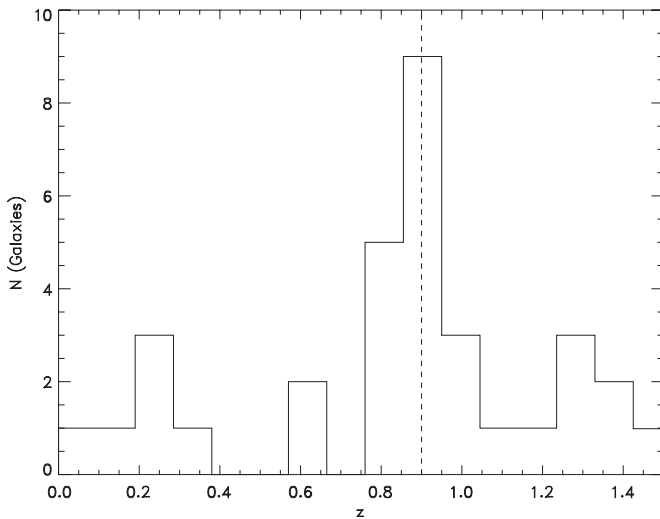


Figure 6. Redshift distribution of the 34 galaxies matched to X-ray point sources in the field of the C11604 supercluster. Two sources at $z = 2.04, 2.30$ fall outside the plot range. We observe a peak in the redshift distribution centered on the mean redshift of the C11604 system, which is denoted by the vertical dashed line.

a null match). This cutoff was reduced to 0.75 for matches with LFC objects to include several well-aligned sources near the completeness limit of the LFC catalog. For sources with more than a single-candidate counterpart, the genuine optical match was defined as the source with $\sum_k P_{k,j} > 0.8$ and $P_{i,j}/\sum_{k \neq i} P_{k,j} > 4$, where k is the set of optical candidates. If no single candidate fulfilled this requirement, yet their summed probabilities exceeded 0.8, we considered all optical objects with $P_{i,j} > 0.2$ as possible counterparts.

Using this prescription we have matched 100 X-ray sources with unique optical counterparts found in our LFC and ACS imaging of C11604. An additional 11 sources were found to have two candidate counterparts, while one source is matched to three optical candidates. A remaining 49 X-ray sources were found to have no likely optical counterpart within the limits of our optical imaging. The X-ray and optical coordinates of the matched sources are listed in Table 4. The table includes source IDs (Column 1), X-ray centroids (Columns 2 and 3), optical centroids (Columns 4 and 5), the probability that the given X-ray source has an optical counterpart ($\sum_k P_{k,j}$; Column 6), the probability that the given optical source is the genuine counterpart ($P_{i,j}$; Column 7), redshift (Column 8), and the Q_{spect} value for the derived redshift (Column 9).

3.4. Supercluster Members

As described in Section 2.3, our extensive spectroscopic database contains redshifts for 1138 galaxies and spectra of 140 stars in the field of the C11604 supercluster. Of the 125 optical sources matched to our X-ray catalog, a total of 42 have spectroscopic information available. All but two of these are sources considered genuine optical matches using the criteria put forth in Section 3.3, while the remaining pair are both one of two candidate counterparts to their respective X-ray source. We have derived reliable redshifts ($Q_{\text{spect}} \geq 3$ and $Q_{\text{spect}} = -1$) for 37 of the 42 sources which have spectroscopy. While redshifts for all sources are listed in Table 4, we only make use of the 35 $Q_{\text{spect}} \geq 3$ redshifts for the following discussion.

We find that two of the X-ray sources have a clear stellar spectrum, while the remaining 35 sources are extragalactic covering the redshift range $0.055 \leq z \leq 2.30$. The redshift

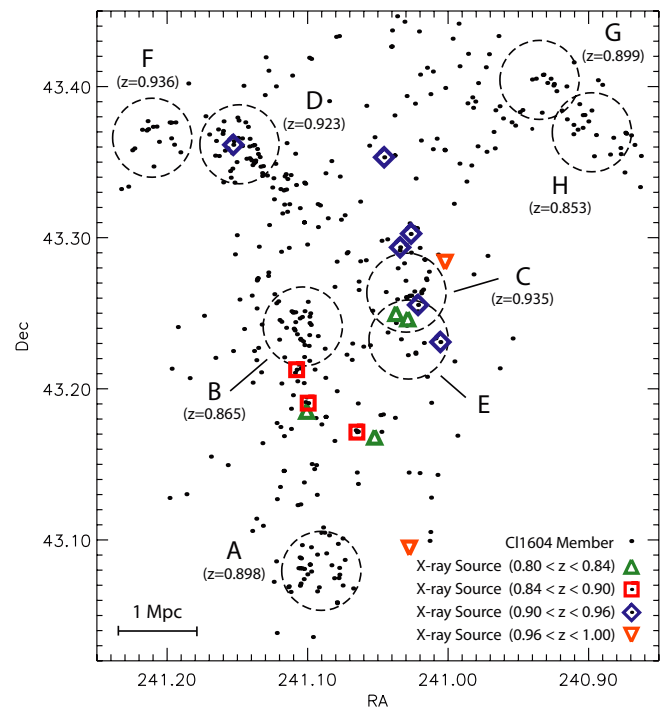


Figure 7. Spatial distribution of the nine X-ray sources that fall within the traditional redshift boundaries of the C11604 supercluster ($0.84 < z < 0.96$). We have split the sample into two redshift bins in order to highlight cluster membership. Also shown are the locations of the four and two sources in the immediate foreground ($0.80 < z < 0.84$) and background ($0.96 < z < 1.00$) of the system, respectively. The cluster labels follow the naming convention of Table 5. See the text for details.

distribution of the extragalactic sources is shown in Figure 6. The distribution exhibits a clear peak at $z = 0.9$, the average redshift of the C11604 supercluster. A total of nine sources have redshifts between $0.84 < z < 0.96$ and fall within the traditional redshift boundaries of the supercluster as defined by Gal & Lubin (2004). An additional six are found in the immediate foreground of the system between $0.80 < z < 0.84$ and another two are found immediately behind the supercluster at $0.96 < z < 1.00$. The remaining sources are high redshift (10 at $z > 1.0$) or foreground sources (nine at $z < 0.8$) seen in projection.

We find that four of the nine supercluster members have hard₁₀-band fluxes between 1 and 2×10^{-14} erg s⁻¹, the flux range where the source excess is observed. The same is true for two of the six sources in the immediate background and foreground of the supercluster, four of the nine sources at $z < 0.8$ and three of the 10 sources at $z > 1.0$. Combined, these sources account for 31% of the sources that contribute to the overdensity, leaving an additional 29 sources with hard₁₀-band fluxes between 1 and 2×10^{-14} erg s⁻¹ for which we do not yet have measured redshifts.

In Figure 7 we plot the spatial distribution of the nine supercluster members and the additional six sources that fall in the immediate foreground and background of the supercluster which may be associated with the large-scale structure of the system. Also shown are the locations and systemic redshifts of individual clusters in the system. We find three supercluster members associated with C11604 + 4314 (hereafter cluster B) at $z = 0.865$; the two sources closest to the cluster center have nearly identical redshifts to that of the cluster ($z = 0.867, 0.871$), while the one with the greatest projected distance is at a higher redshift ($z = 0.899$). The two sources found in

Table 4
Catalog of the 112 X-Ray Sources Matched to Optical Counterparts

Source Name	X-Ray R.A. (J2000)	X-Ray Decl. (J2000)	Optical R.A. (J2000)	Optical Decl. (J2000)	$\Sigma_k P_{k,j}$	$P_{i,j}$	z	Spect. Qual.
J160310.5+432627	16:03:10.5	43:26:27.3	16:03:10.3	43:26:27.7	0.951	0.951		
J160316.9+432256	16:03:16.9	43:22:56.3	16:03:16.9	43:22:54.7	0.972	0.833		
J160324.9+432226	16:03:24.9	43:22:26.2	16:03:24.8	43:22:26.3	0.997	0.990	1.118	4
J160329.4+432059	16:03:29.4	43:20:59.5	16:03:29.3	43:21:00.1	0.963	0.766	...	1
J160332.4+431953	16:03:32.4	43:19:53.1	16:03:32.5	43:19:53.0	0.944	0.944		
J160337.1+431331	16:03:37.1	43:13:31.6	16:03:37.2	43:13:31.4	0.882	0.882		
J160337.3+431625	16:03:37.3	43:16:25.3	16:03:37.2	43:16:26.4	0.901	0.901		
J160338.8+431108	16:03:38.8	43:11:08.0	16:03:38.7	43:11:08.2	0.807	0.807		
J160339.2+431902	16:03:39.2	43:19:02.8	16:03:39.1	43:19:03.4	0.785	0.785		
J160339.6+431601	16:03:39.6	43:16:01.1	16:03:39.6	43:16:02.4	0.962	0.962		
J160339.7+432023	16:03:39.7	43:20:23.7	16:03:39.7	43:20:24.4	0.966	0.966	0.270	3
J160340.6+431752	16:03:40.6	43:17:52.4	16:03:40.6	43:17:52.2	0.984	0.984		
J160341.4+431649	16:03:41.4	43:16:49.8	16:03:41.5	43:16:49.7	0.973	0.973		
J160342.8+431117	16:03:42.8	43:11:17.0	16:03:42.8	43:11:16.9	0.993	0.993		
J160343.7+433007	16:03:43.7	43:30:07.3	16:03:43.7	43:30:07.0	0.886	0.479		
J160343.7+433007			16:03:44.0	43:30:03.6	0.886	0.200		
J160343.7+433007			16:03:44.2	43:30:08.3	0.886	0.207		
J160345.3+431824	16:03:45.3	43:18:24.9	16:03:45.5	43:18:23.6	0.833	0.473		
J160345.3+431824			16:03:45.4	43:18:25.1	0.833	0.360		
J160345.3+431507	16:03:45.3	43:15:07.7	16:03:45.0	43:15:07.4	0.993	0.993		
J160348.8+431717	16:03:48.8	43:17:17.3	16:03:48.7	43:17:17.8	0.918	0.918		
J160350.8+432123	16:03:50.8	43:21:23.1	16:03:50.8	43:21:23.2	0.955	0.955		
J160353.7+432752	16:03:53.7	43:27:52.2	16:03:53.7	43:27:52.0	0.982	0.982		
J160356.2+431317	16:03:56.2	43:13:17.9	16:03:56.2	43:13:18.0	0.989	0.989	0.593	4
J160356.7+432358	16:03:56.7	43:23:58.9	16:03:56.7	43:23:59.0	0.997	0.997		
J160356.9+430734	16:03:56.9	43:07:34.0	16:03:56.9	43:07:34.5	0.945	0.945		
J160356.9+430950	16:03:56.9	43:09:50.9	16:03:56.9	43:09:50.6	0.984	0.984		
J160357.5+432349	16:03:57.5	43:23:49.8	16:03:57.4	43:23:49.9	0.998	0.998		
J160358.4+430513	16:03:58.4	43:05:13.2	16:03:58.5	43:05:14.1	0.981	0.981		
J160359.9+431142	16:03:59.9	43:11:42.7	16:03:59.9	43:11:42.9	0.990	0.990	0.777	4
J160400.1+432231	16:04:00.1	43:22:31.3	16:04:00.1	43:22:31.4	0.990	0.508		
J160400.1+432231			16:04:00.1	43:22:30.9	0.990	0.482	1.399	4
J160400.2+430947	16:04:00.2	43:09:47.9	16:04:00.2	43:09:47.9	0.985	0.985		
J160400.5+431706	16:04:00.5	43:17:06.2	16:04:00.6	43:17:06.6	0.948	0.948	0.979	4
J160401.0+431153	16:04:01.0	43:11:53.0	16:04:01.0	43:11:53.3	0.930	0.930	1.237	4
J160401.3+431351	16:04:01.3	43:13:51.2	16:04:01.3	43:13:51.4	0.989	0.989	0.927	4
J160402.1+431333	16:04:02.1	43:13:33.6	16:04:02.1	43:13:33.5	0.998	0.998	0.349	4
J160404.3+431013	16:04:04.3	43:10:13.8	16:04:04.3	43:10:13.6	0.985	0.985		
J160404.6+432906	16:04:04.6	43:29:06.3	16:04:04.7	43:29:06.5	0.993	0.993		
J160405.1+431519	16:04:05.1	43:15:19.4	16:04:05.1	43:15:19.8	0.968	0.968	0.935	4
J160405.3+432110	16:04:05.3	43:21:10.7	16:04:05.3	43:21:11.2	0.990	0.990	1.208	4
J160405.4+431122	16:04:05.4	43:11:22.0	16:04:05.4	43:11:22.0	0.914	0.914		
J160405.6+432351	16:04:05.6	43:23:51.6	16:04:05.6	43:23:51.9	0.992	0.912	...	1
J160405.9+433128	16:04:05.9	43:31:28.6	16:04:06.0	43:31:28.6	0.909	0.909		
J160406.0+431807	16:04:06.0	43:18:07.6	16:04:06.1	43:18:08.0	0.976	0.811	0.913	3
J160406.1+430532	16:04:06.1	43:05:32.8	16:04:06.1	43:05:31.8	0.985	0.985		
J160406.3+432125	16:04:06.3	43:21:25.8	16:04:06.3	43:21:26.1	0.999	0.999	2.040	4
J160406.6+430545	16:04:06.6	43:05:45.3	16:04:06.6	43:05:44.5	0.982	0.982	0.970	4
J160407.0+431445	16:04:07.0	43:14:45.8	16:04:07.0	43:14:46.0	0.997	0.997	0.808	4
J160407.5+432640	16:04:07.5	43:26:40.0	16:04:07.5	43:26:40.3	0.993	0.993	1.285	4
J160408.0+431736	16:04:08.0	43:17:36.4	16:04:08.2	43:17:36.9	0.988	0.947	0.937	4
J160408.9+431456	16:04:08.9	43:14:56.0	16:04:08.9	43:14:56.2	0.999	0.999	0.809	4
J160408.9+431825	16:04:08.9	43:18:25.8	16:04:08.9	43:18:26.5	0.971	0.971	1.285	4
J160409.0+431307	16:04:09.0	43:13:07.1	16:04:08.9	43:13:05.6	0.994	0.994	0.131	4
J160409.7+432341	16:04:09.7	43:23:41.3	16:04:09.7	43:23:41.6	0.946	0.946		
J160410.0+430437	16:04:10.0	43:04:37.2	16:04:10.0	43:04:37.6	0.989	0.989	0.669	2
J160410.2+432614	16:04:10.2	43:26:14.6	16:04:10.2	43:26:15.0	0.999	0.999		
J160410.9+432111	16:04:10.9	43:21:11.0	16:04:10.9	43:21:10.6	0.994	0.624		
J160410.9+432111			16:04:10.9	43:21:11.0	0.994	0.342	0.935	4
J160411.4+432733	16:04:11.4	43:27:33.5	16:04:11.5	43:27:33.2	0.858	0.858	0.779	2
J160411.5+430148	16:04:11.5	43:01:48.2	16:04:11.6	43:01:49.7	0.999	0.957		
J160412.6+431002	16:04:12.6	43:10:02.1	16:04:12.7	43:10:02.2	0.975	0.975	0.829	4
J160412.8+432627	16:04:12.8	43:26:27.8	16:04:12.8	43:26:28.4	0.999	0.999		
J160413.1+430927	16:04:13.1	43:09:27.6	16:04:13.2	43:09:27.2	0.982	0.982	0.600	4
J160415.5+431016	16:04:15.5	43:10:16.6	16:04:15.6	43:10:16.8	0.994	0.994	0.899	4

Table 4
(Continued)

Source Name	X-Ray R.A. (J2000)	X-Ray Decl. (J2000)	Optical R.A. (J2000)	Optical Decl. (J2000)	$\Sigma_k P_{k,j}$	$P_{i,j}$	z	Spect. Qual.
J160415.6+431410	16:04:15.6	43:14:10.5	16:04:15.6	43:14:10.8	0.950	0.496		
J160415.6+431410			16:04:15.5	43:14:10.7	0.950	0.454		
J160415.8+433120	16:04:15.8	43:31:20.8	16:04:16.0	43:31:22.3	0.851	0.797		
J160416.2+431419	16:04:16.2	43:14:19.1	16:04:16.2	43:14:19.3	0.998	0.998	-0.004	-1
J160416.6+432440	16:04:16.6	43:24:40.5	16:04:16.6	43:24:41.1	0.963	0.890		
J160417.5+433025	16:04:17.5	43:30:25.1	16:04:17.5	43:30:25.8	0.982	0.982		
J160418.2+430018	16:04:18.2	43:00:18.3	16:04:18.7	43:00:12.4	0.977	0.929		
J160418.2+431925	16:04:18.2	43:19:25.5	16:04:18.2	43:19:26.2	0.999	0.999		
J160419.1+431104	16:04:19.1	43:11:04.3	16:04:19.1	43:11:04.4	0.996	0.996	1.424	4
J160419.2+431600	16:04:19.2	43:16:00.5	16:04:19.3	43:16:01.1	0.972	0.968	1.437	4
J160421.1+431521	16:04:21.1	43:15:21.4	16:04:21.1	43:15:22.0	0.887	0.887		
J160421.8+432354	16:04:21.8	43:23:54.7	16:04:21.8	43:23:55.0	0.998	0.998	0.055	4
J160423.9+431125	16:04:23.9	43:11:25.9	16:04:23.9	43:11:25.9	0.996	0.996	0.867	4
J160423.9+431610	16:04:23.9	43:16:10.3	16:04:23.9	43:16:10.6	0.976	0.976	2.304	4
J160424.1+431106	16:04:24.1	43:11:06.2	16:04:24.1	43:11:06.6	0.992	0.992	0.824	4
J160424.2+433421	16:04:24.2	43:34:21.1	16:04:23.0	43:34:20.9	0.992	0.834		
J160425.2+430133	16:04:25.2	43:01:33.5	16:04:25.3	43:01:31.3	0.939	0.845	0.255	4
J160425.9+431245	16:04:25.9	43:12:45.2	16:04:25.9	43:12:45.5	0.996	0.996	0.871	4
J160426.1+430755	16:04:26.1	43:07:55.0	16:04:26.1	43:07:54.7	0.986	0.986	1.035	4
J160426.3+431742	16:04:26.3	43:17:42.3	16:04:26.4	43:17:43.5	0.982	0.586		
J160426.3+431742			16:04:26.4	43:17:43.0	0.982	0.288		
J160427.5+432252	16:04:27.5	43:22:52.5	16:04:27.5	43:22:53.1	0.999	0.999	0.278	4
J160428.3+430940	16:04:28.3	43:09:40.8	16:04:28.3	43:09:41.2	0.901	0.901		
J160429.1+432830	16:04:29.1	43:28:30.1	16:04:29.1	43:28:30.2	0.947	0.947		
J160429.5+432306	16:04:29.5	43:23:06.8	16:04:29.5	43:23:06.9	0.921	0.617		
J160429.5+432306			16:04:29.5	43:23:07.2	0.921	0.304		
J160431.4+432954	16:04:31.4	43:29:54.7	16:04:31.3	43:29:55.2	0.947	0.947		
J160432.7+430802	16:04:32.7	43:08:02.4	16:04:32.8	43:08:02.7	0.998	0.998		
J160433.3+430339	16:04:33.3	43:03:39.4	16:04:33.3	43:03:39.5	0.994	0.994		
J160433.8+431833	16:04:33.8	43:18:33.0	16:04:33.8	43:18:33.5	0.999	0.999		
J160433.8+432352	16:04:33.8	43:23:52.4	16:04:33.8	43:23:52.5	0.957	0.957		
J160435.5+432112	16:04:35.5	43:21:12.3	16:04:35.5	43:21:12.2	0.984	0.606		
J160435.5+432112			16:04:35.5	43:21:13.3	0.984	0.203		
J160435.8+430551	16:04:35.8	43:05:51.8	16:04:35.9	43:05:51.7	0.872	0.773		
J160436.0+431929	16:04:36.0	43:19:29.3	16:04:36.0	43:19:29.6	0.996	0.970		
J160436.7+432141	16:04:36.7	43:21:41.4	16:04:36.7	43:21:41.3	0.998	0.998	0.923	4
J160437.5+432010	16:04:37.5	43:20:10.2	16:04:37.5	43:20:11.4	0.997	0.997		
J160438.3+432625	16:04:38.3	43:26:25.2	16:04:38.3	43:26:24.1	0.872	0.872		
J160438.4+430729	16:04:38.4	43:07:29.1	16:04:38.5	43:07:29.3	0.990	0.990		
J160441.7+432057	16:04:41.7	43:20:57.8	16:04:41.7	43:20:58.2	0.978	0.807	0.991	2
J160443.3+431348	16:04:43.3	43:13:48.2	16:04:43.3	43:13:48.3	0.997	0.997		
J160444.6+432026	16:04:44.6	43:20:26.8	16:04:44.6	43:20:27.4	0.999	0.500		
J160444.6+432026			16:04:44.6	43:20:27.0	0.999	0.500		
J160446.0+432234	16:04:46.0	43:22:34.5	16:04:46.0	43:22:34.8	0.998	0.998	0.002	-1
J160448.4+430807	16:04:48.4	43:08:07.3	16:04:48.5	43:08:07.2	0.995	0.995		
J160449.5+430723	16:04:49.5	43:07:23.4	16:04:49.5	43:07:23.4	0.780	0.780		
J160450.2+432158	16:04:50.2	43:21:58.3	16:04:50.2	43:21:58.8	0.999	0.999		
J160451.3+431548	16:04:51.3	43:15:48.8	16:04:51.3	43:15:49.2	0.979	0.979		
J160453.3+431912	16:04:53.3	43:19:12.2	16:04:53.3	43:19:11.6	0.947	0.947		
J160455.5+431445	16:04:55.5	43:14:45.3	16:04:55.5	43:14:42.4	0.967	0.602		
J160455.5+431445			16:04:55.6	43:14:44.9	0.967	0.365		
J160456.9+432037	16:04:56.9	43:20:37.2	16:04:56.8	43:20:34.2	0.809	0.464		
J160456.9+432037			16:04:57.0	43:20:37.3	0.809	0.247		
J160459.6+430508	16:04:59.6	43:05:08.2	16:04:59.6	43:05:07.2	0.830	0.454		
J160459.6+430508			16:04:59.5	43:05:11.9	0.830	0.376		
J160459.8+431957	16:04:59.8	43:19:57.3	16:04:59.9	43:19:58.0	0.855	0.855		
J160500.3+431028	16:05:00.3	43:10:28.0	16:05:00.3	43:10:27.9	0.994	0.994		
J160501.1+430724	16:05:01.1	43:07:24.1	16:05:01.1	43:07:23.8	0.780	0.780		
J160505.1+430632	16:05:05.1	43:06:32.5	16:05:05.2	43:06:32.3	0.909	0.669		
J160506.5+431032	16:05:06.5	43:10:32.7	16:05:06.6	43:10:36.2	0.985	0.985		

(This table is also available in a machine-readable form in the online journal.)

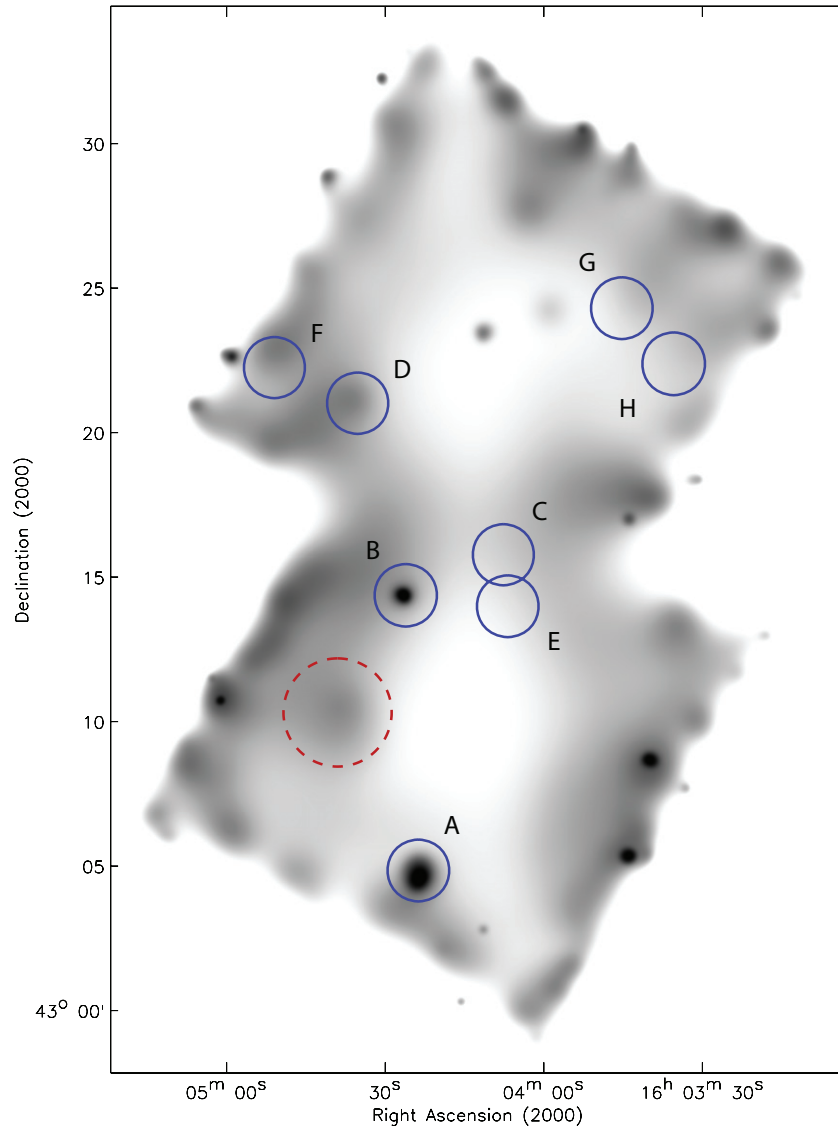


Figure 8. Extended emission in the field of the CL1604 supercluster in the 0.5–2.0 keV band. All point sources detected with *wavdetect* were removed and the image adaptively smoothed with a minimal smoothing scale of $10''$. The locations of eight red-galaxy overdensities, seven of which are spectroscopically confirmed galaxy clusters or groups in the supercluster, are circled and labeled following the naming convention of Gal et al. (2008) and that of Table 5. The circles have a radius of $0.5 h_{70}^{-1}$ Mpc at the cluster redshifts. A serendipitously detected foreground cluster at $z = 0.3$ is noted by the dashed circle. (A color version of this figure is available in the online journal.)

the foreground of cluster B are themselves clustered in redshift space at $z = 0.828, 0.824$. Near CL1604 + 4316 (cluster C) at $z = 0.935$, we find four nearby sources that are associated in redshift space having $z = 0.927, 0.935, 0.937, 0.935$. An additional source is located in the foreground of the cluster at $z = 0.913$. In CL1604 + 4321 (cluster D), we find one source with a redshift identical to that of the systemic cluster redshift of $z = 0.923$.

Despite the high galaxy density and extensive spectroscopic coverage of CL1604 + 4304 (cluster A), we find no sources associated with the system. The cluster is the richest system in the CL1604 association and it is also the most X-ray luminous. We also do not find any sources near the center of cluster B, with the nearest source roughly $1 h_{70}^{-1}$ Mpc from the cluster center. As we discuss in Section 4, these systems are the only clusters for which we detect diffuse emission. Although this emission effectively raises our point-source detection threshold in the soft band, the emission is of relatively low level and would only mask the faintest of sources. For example, in the

center of cluster A we find that the flux limit for a 3σ detection rises to 1.13×10^{-15} erg s $^{-1}$ in the soft band. Therefore, the diffuse emission from these systems does not prevent us from detecting bright point sources in the soft band, nor does it affect our ability to detect sources in the hard band, yet none are found, either with *wavdetect* or by visual inspection. This is quite unlike clusters C and D, in which we find sources near the center of each system (both in projection and redshift space). This observation is consistent with the results of Gilmour et al. (2007) who found that AGN avoided the densest regions of the low-redshift supercluster Abell 901/902.

It is interesting to note that Gal et al. (2008) found that clusters B and D showed evidence for velocity segregation in the redshift distribution of their member galaxies, indicating they may have undergone a recent merger event or have a significant population of actively accreting galaxies. This is quite unlike cluster A, which is the most relaxed system in the supercluster. The difference in the dynamical activity of clusters A and B indicate that the global properties of these systems may affect the

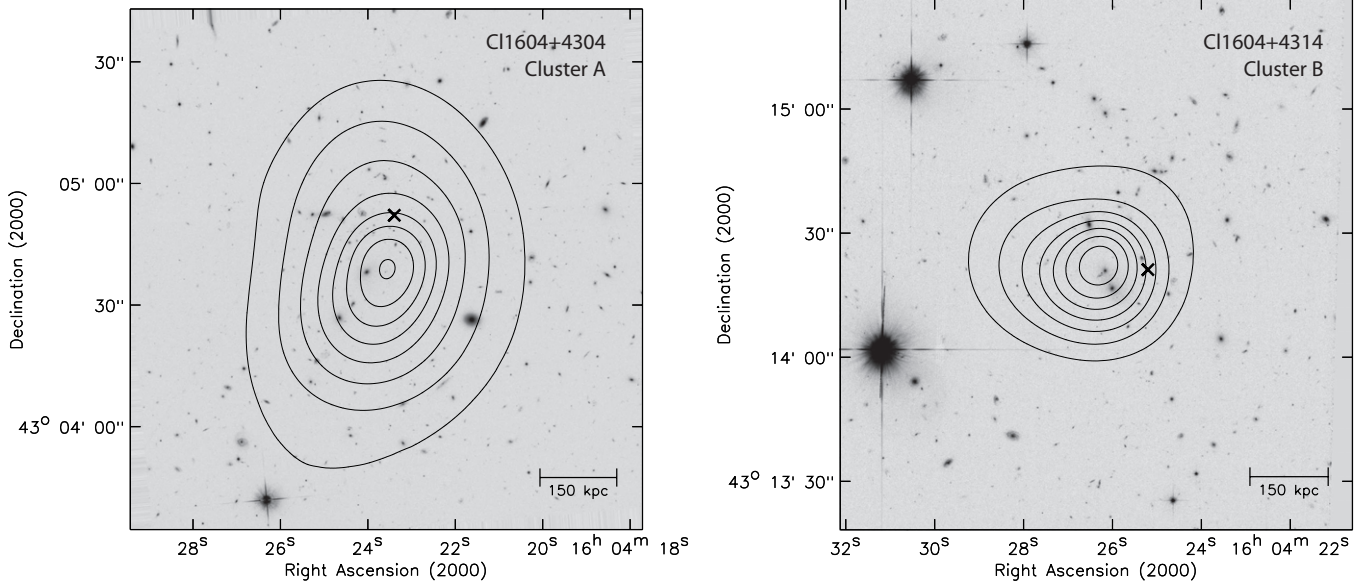


Figure 9. Optical imaging from *HST* of the two Cl1604 clusters (A and B) detected in our *Chandra* imaging with contours of their diffuse X-ray emission overlaid. The contour levels begin at 1.25 times the local background and are logarithmically spaced thereafter. The optical centroids of each cluster, derived as the median position of the cluster’s confirmed members, are marked by the crosses in each panel. The optical images shown are in the F814W filter and have a pixel scale of $0''.03 \text{ pixel}^{-1}$.

level of AGN activity observed in each cluster. In a forthcoming paper, we will discuss the environments and optical properties of the supercluster members in greater detail, including the local galaxy density near the host galaxies and the global properties of the clusters within which they reside. This future study will further explore the possibility that cluster properties, such as increased dynamical activity or the presence of a significant intracluster medium (ICM), can affect the level of AGN activity observed in a system.

4. DIFFUSE X-RAY EMISSION

A total of 10 red-galaxy overdensities were detected in our LFC imaging of the Cl1604 field (Gal et al. 2008), of which eight fall within the FOV of our ACIS-I imaging. The optical properties and velocity dispersions of these galaxy clusters and groups are discussed in detail in Gal et al. (2005, 2008). We searched for diffuse X-ray emission at the location of each overdensity and found significant ($>3\sigma$) emission above the background near clusters A and B. An increased X-ray background in the soft band was detected near cluster D and Cl1605 + 4322 (hereafter cluster F), but at a much reduced significance level. For cluster C, Cl1604 + 4324 (cluster G), and Cl1604 + 4322 (cluster H), we find no emission in excess of the background. The galaxy overdensity Cl1604 + 4314B (system E), which is likely to be the superposition of supercluster members at various redshifts (see Gal et al. 2008), is also not detected as expected. The diffuse emission detected from the Cl1604 systems is shown in Figure 8, which displays an adaptively smoothed, soft-band image of the supercluster field where we have replaced all point sources detected by *wavdetect* with an estimate of the local background using *dmfilth* prior to smoothing. Contours of the X-ray emission from clusters A and B are also plotted overtop *HST/ACS* imaging of the systems in the F814W band in Figure 9.

To quantify the extent, count rate and significance above the background of the emission from clusters A and B, we employed a growth curve analysis on the soft-band counts from each cluster. Azimuthally averaged surface-brightness profiles were

constructed for each system by summing the counts in annuli centered on the peak of the diffuse emission. The background level of each field was then set to the median of the source-free, outer portions of the profile. A cumulative net count profile was then constructed by measuring the counts in successively larger apertures centered on the diffuse emission and subtracting an appropriately scaled background. We take the total number of counts originating from the cluster to be the level at which the cumulative profile ceases to grow. The cumulative net count profiles for the two clusters are shown in Figure 10. We detect a total of 133.9 and 76.3 net counts⁸ in the soft band within an extent of $80''$ and $50''$ (0.62 and $0.39 h_{70}^{-1} \text{ Mpc}$) from clusters A and B at a significance level of 7.20σ and 6.21σ , respectively.

Despite the low number counts, we determined the temperature and X-ray luminosity of each system by fitting a Raymond–Smith thermal plasma model to the energy spectra of the diffuse emission. The spectra were extracted out to the measured extent of each system with the CIAO task *specextract*, and the background was measured in a local annulus surrounding the extraction region. The spectra were grouped to contain at least 15 counts per bin and fitted with the *Sherpa* package using a χ^2 -statistic with the Gehrels (1986) approximation of errors given the low number counts. The metal abundance was fixed at $0.3 Z_{\odot}$ and only the temperatures of the systems were allowed to float. The fit was carried out over 0.3–8 keV, but we found our results to be robust against variations to this energy range. Our extracted spectra and resulting best fits are shown in Figure 11. We find temperatures of $3.50^{+1.82}_{-1.08}$ and $1.64^{+0.65}_{-0.45}$ keV for clusters A and B, respectively; the estimated confidence intervals are 1σ and were derived through projection of the statistic surface using the *proj* task in *Sherpa*. Cluster A was previously observed with *XMM-Newton* and we find that our best-fit temperature for the system is higher than the $2.51^{+1.05}_{-0.69}$ keV reported by Lubin et al. (2004), but consistent given the errors on both estimates. The resulting bolometric luminosities for clusters A and B are 1.43×10^{44} and $8.20 \times$

⁸ The quoted values are vignetting-corrected counts above the background.

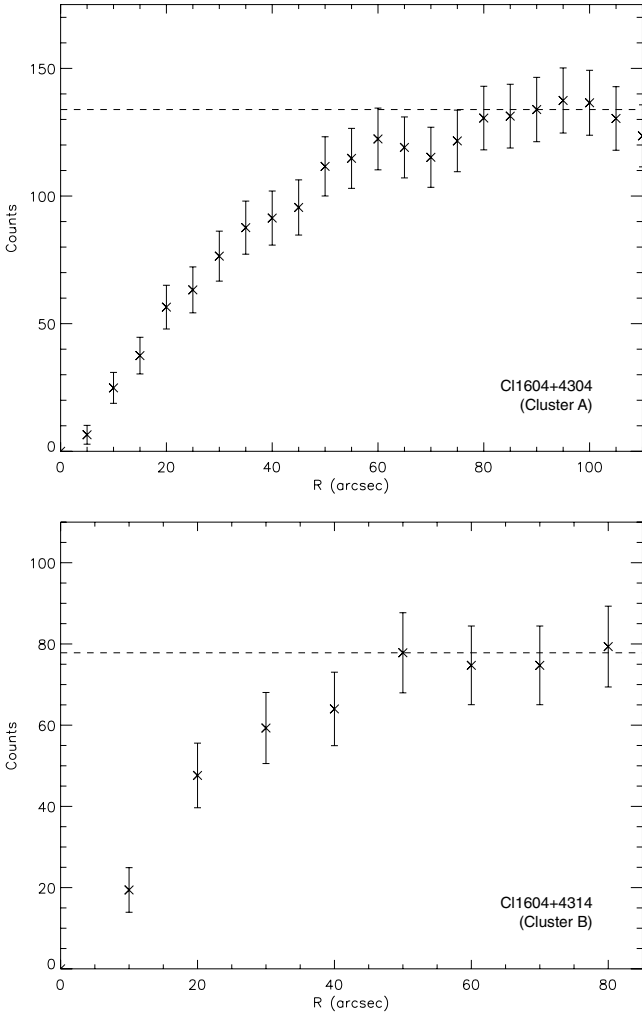


Figure 10. Cumulative net count profiles for clusters A and B. The total number of counts originating from each cluster is shown by the horizontal dashed line.

$10^{43} h_{70}^{-2} \text{ erg s}^{-1}$, respectively, within an extent of $80''$ and $50''$. If we assume that the cluster surface-brightness profiles follow a β -model with the canonical parameters $\beta = 2/3$ and $r_c = 180 h_{70}^{-1} \text{ kpc}$, the measurement apertures enclose 90.9% and 70.5% of the total flux out to the R_{200} radius of each cluster. We determined R_{200} as $R_{200} = 2\sigma_v / \sqrt{200H(z)}$ using the velocity dispersions measured by Gal et al. (2008); the resulting radii are $110''$ and $126''$. Extrapolating the observed emission out to R_{200} , clusters A and B have bolometric luminosities of 1.58×10^{44} and $1.16 \times 10^{44} h_{70}^{-2} \text{ erg s}^{-1}$, respectively. Our best-fit temperatures and the resulting fluxes and luminosities of the two clusters are summarized in Table 5.

The remaining five clusters show no statistically significant emission in excess of the background and are therefore treated as nondetections. We calculated upper limits to the counts from each system as the 3σ Poissonian fluctuation of the background measured within a $0.5 h_{70}^{-1} \text{ Mpc}$ radius aperture centered on the system's optical centroid from Gal et al. (2008). While we do observe a slightly increased background at the positions of clusters D and F, the measured counts are less than that expected from a 3σ Poissonian fluctuation, therefore we treat both systems as nondetections. The 3σ upper limit to the counts from each cluster is listed in Table 5. We converted count rates to flux by normalizing a Raymond–Smith thermal plasma model in Sherpa to the measured upper limits for

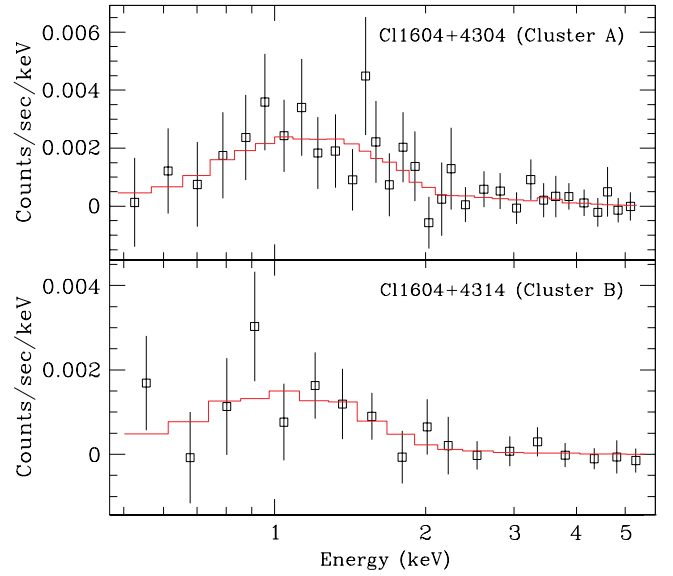


Figure 11. Spectral fits to the observed energy spectra of clusters A and B. The spectra have been background subtracted and grouped to contain at least 15 counts per bin. The best-fit Raymond–Smith thermal spectra have temperatures of 3.5 and 1.6 keV for clusters A and B, respectively.

(A color version of this figure is available in the online journal.)

each system, with the appropriate instrument response files obtained using `specextract` at the location of each cluster. We assumed a $0.3Z_{\odot}$ metallicity and a temperature of 2 keV for all systems. The resulting upper limits to the flux and luminosities of each system are listed in Table 5. We note that had we iteratively solved for the cluster temperatures using the L_x – T relationship as opposed to using a fixed 2 keV value, the resulting temperatures would have ranged from 2.4 to 2.6 keV. The change would reduce our luminosity upper limits by less than 1%.

4.1. Cluster Scaling Relations

It was previously reported by Lubin et al. (2004, hereafter L04) that cluster A and the optically selected cluster C11324+3011 at $z = 0.76$ were found to be underluminous compared to their high-redshift, X-ray-selected counterparts with similar galaxy velocity dispersions. The systems were also found to deviate from the σ_v – T relationship at the $\sim 4\sigma$ level, exhibiting significantly cooler ICM temperatures than expected from local scaling relationships. These observations hinted at the intriguing possibility that optical cluster selection at high redshift may preferentially select younger systems that have yet to assemble a significant ICM or undergo a major phase of nongravitational heating. In this section, we revisit this issue using the results of our *Chandra* observations and newly determined velocity dispersions for the C11604 systems from Gal et al. (2008).

4.1.1. The L_x – T Relation

If the thermodynamics of a cluster's ICM is governed solely by gravitational processes, the self-similar description of clusters predicts that the X-ray luminosity should scale with ICM temperature as $L \propto T^2$, given that the gas radiates via bremsstrahlung emission (Kaiser 1986). Furthermore, the evolution of this relationship is expected to follow the evolution of the Hubble parameter which goes as

$$E(z) = [\Omega_m(1+z)^3 + (1 - \Omega_m - \Omega_{\Lambda})(1+z)^2 + \Omega_{\Lambda}]^{1/2}. \quad (10)$$

Table 5
X-Ray Properties of Galaxy Clusters in the C11604 supercluster

Cluster	R.A. (J2000) ^a	Decl. (J2000) ^a	z	Extent (h_{70}^{-1} kpc arcsec ⁻¹)	Net Cnts	T_x (keV)	F_x (0.5–2 keV) ($\times 10^{-15}$) ^b	L_x (Bol) ($\times 10^{43}$) ^c	L_x (Bol) ($\times 10^{43}$; R_{200}) ^d
C11604 + 4304 (A)	241.097473	43.081150	0.898	623/80''	134	$3.50^{+1.82}_{-1.08}$	14.76	14.33	15.76
C11604+4314 (B)	241.105011	43.239220	0.865	385/50''	76	$1.64^{+0.65}_{-0.45}$	9.26	8.20	11.64
C11604+4316 (C)	241.031623	43.263130	0.935	500/63.5''	<44	2	<7.20	<7.59	<5.50
C11604+4321 (D)	241.138651	43.353430	0.923	500/63.7''	<47	2	<7.84	<8.02	<9.10
C11605+4322 (F)	241.213137	43.370908	0.936	500/63.5''	<46	2	<7.83	<8.31	<9.19
C11604+4324 (G)	240.937542	43.405199	0.899	500/64.2''	<46	2	<7.79	<7.38	<7.35
C11604+4322 (H)	240.896481	43.373087	0.853	500/65.2''	<42	2	<7.03	<5.85	<4.17

Notes.

^a Cluster centroids determined as the median redshift of member galaxies within $1 h_{70}^{-1}$ Mpc.

^b In units of $\text{erg s}^{-1} \text{cm}^{-2}$.

^c In units of $h_{70}^{-2} \text{erg s}^{-1}$.

^d In units of $h_{70}^{-2} \text{erg s}^{-1}$; assuming $\beta = 2/3$ and $r_c = 180 h_{70}^{-1}$ kpc.

In actuality, several studies have shown that clusters exhibit hotter ICM temperatures than expected from the self-similar relationship, suggesting nongravitational processes such as AGN feedback has injected energy into the systems. Low-redshift cluster surveys have found that the L_x – T relationship follows a form closer to $L \propto T^3$ (Markevitch 1998; Xue & Wu 2000; Vikhlinin et al. 2002). On the other hand, although clusters do not obey the predicted L_x – T relationship, studies show that the evolution of the correlation does indeed follow the expected self-similar evolution. Maughan et al. (2006) have shown that when self-similar evolution is taken into account, the properties of X-ray-selected WARPS clusters out to $z \sim 1$ agree with the low-redshift L_x – T relationship, indicating that the processes which heat the ICM beyond the self-similar prediction occur at an even earlier epoch or in dynamically younger clusters (see also Vikhlinin et al. 2002 and Hicks et al. 2006).

In Figure 12, we plot the bolometric X-ray luminosity of clusters A and B extrapolated out to their R_{200} radii against their ICM temperatures. Also shown are other high-redshift, X-ray and optically selected clusters drawn from the literature. We have corrected each system for the predicted self-similar evolution and overplotted the local L_x – T relationship of Markevitch (1998), which has a power-law slope of 2.64. The optically selected clusters are drawn from the ESO Distant Cluster Survey (EDisCS; White et al. 2005; Johnson et al. 2006) and the Red Sequence Cluster Survey (RCS; Gladders & Yee 2005; Hicks et al. 2007), while the X-ray-selected sample includes clusters from the MACS (Ebeling et al. 2001a, 2007) and several individual clusters drawn from a variety of studies (Borgani et al. 1999; Donahue et al. 1999; Gioia et al. 1999; Tran et al. 1999; Ebeling et al. 2001b; Holden et al. 2001; Stanford et al. 2001, 2002; Vikhlinin et al. 2002; Valtchanov et al. 2004; Maughan et al. 2004; Rosati et al. 2004; Mullis et al. 2005; Hilton et al. 2007; Demarco et al. 2007).

In agreement with the results of L04 we find that the optically selected clusters A and B are consistent with the L_x – T relationship followed by high-redshift, X-ray-selected systems. The same is largely true for the optically selected EDisCs and RCS clusters, as previously reported. While we find that cluster B deviates from the best-fit relationship of Markevitch (1998) at the 2.0σ level, it is well within the cluster-to-cluster scatter observed in the correlation. Figure 12 suggests that while optical selection of clusters at high redshift often finds clusters further down the luminosity (and hence mass) function, it does not preferentially select systems that deviate from the predicted scaling relationships between cluster X-ray properties.

4.1.2. The σ_v – T Relation

L04 found that while the X-ray properties of their optically selected clusters were consistent with X-ray–X-ray scaling relations, they strongly deviated from X-ray–optical relations, such as the σ_v – T correlation. If the gas which makes up the ICM shares the same dynamics as the cluster galaxies, it is expected that the ICM temperature should be related to galaxy velocity dispersion as $\sigma_v \propto T^{1/2}$. L04 reported that their optically selected clusters had cooler temperatures than expected given their measured velocity dispersions. The deviations were at the 4σ and 5σ levels for C11324 + 3011 and cluster A, respectively. We revisit this issue with an improved velocity dispersion for cluster A and the first ever X-ray observations of cluster B in the C11604 system.

Since the publication of the L04 results, our spectroscopic data set for cluster A has substantially improved (see Gal et al. 2008), allowing us to update the original estimate of its velocity dispersion. Using a 3σ iterative clipping technique on 32 redshifts within $1 h_{70}^{-1}$ Mpc of the cluster center, we measure a velocity dispersion of $619 \pm 96 \text{ km s}^{-1}$ for the system. Our revised value is significantly lower than the L04 estimate of 1226 km s^{-1} determined from a sample of 22 galaxies within a $2' \times 8'$ region centered on the cluster. Using the same procedure on galaxies in cluster B, we obtain a velocity dispersion of $811 \pm 76 \text{ km s}^{-1}$ for the system.

In Figure 13, we plot the galaxy velocity dispersion versus ICM temperature of the two detected C11604 clusters, as well as several high-redshift X-ray and optically selected clusters drawn from the literature. Also shown in the background are clusters from a large sample of 273 low-to-moderate redshift systems observed with *ASCA* and uniformly analyzed by Horner (2001). Their best-fit σ_v – T relationship using this data set is plotted as the dashed line. Alternatively the solid line shows the best fit from Xue & Wu (2000), who used a slightly larger sample of clusters drawn from the literature and observed using a variety of instruments.

Using our revised velocity dispersion for cluster A, we find the system is now in very good agreement with the σ_v – T relation found at low redshifts and followed by high-redshift, X-ray-selected systems. The same is largely true for the two EDisCs and three RCS clusters which have published velocity dispersions. The exception to this is cluster B which deviates significantly from both the Xue & Wu (2000) and Horner (2001) best-fit relations. The deviation is significant at roughly the 4σ level (without taking into account the observed scatter).

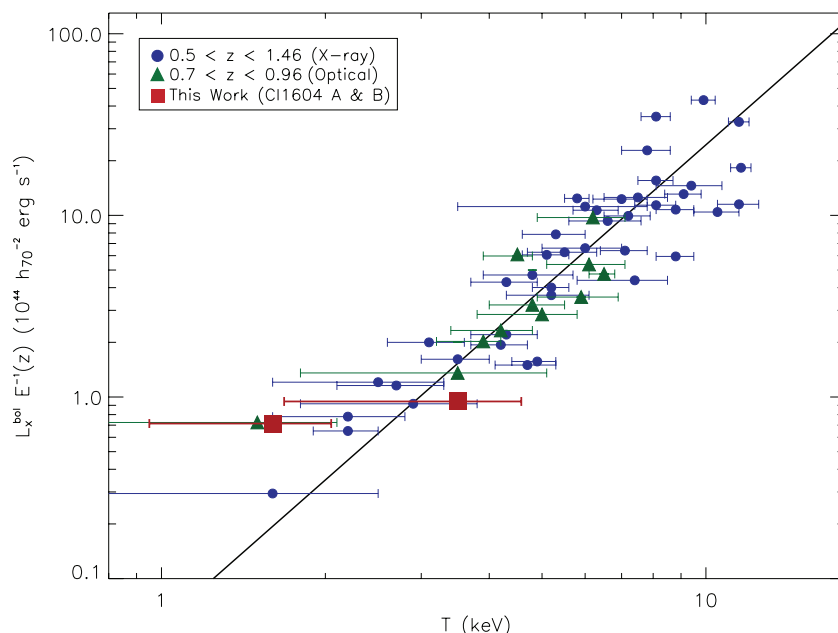


Figure 12. Relation between bolometric luminosity and ICM temperature for clusters at $z \geq 0.5$ scaled to account for self-similar evolution. The filled squares indicate the two optically selected clusters detected in the Cl1604 supercluster, while the circles and triangles denote X-ray and optically selected high-redshift clusters, respectively, drawn from the literature. The solid line represents the best fit of Markevitch (1998) to the correlation observed in low-redshift clusters.

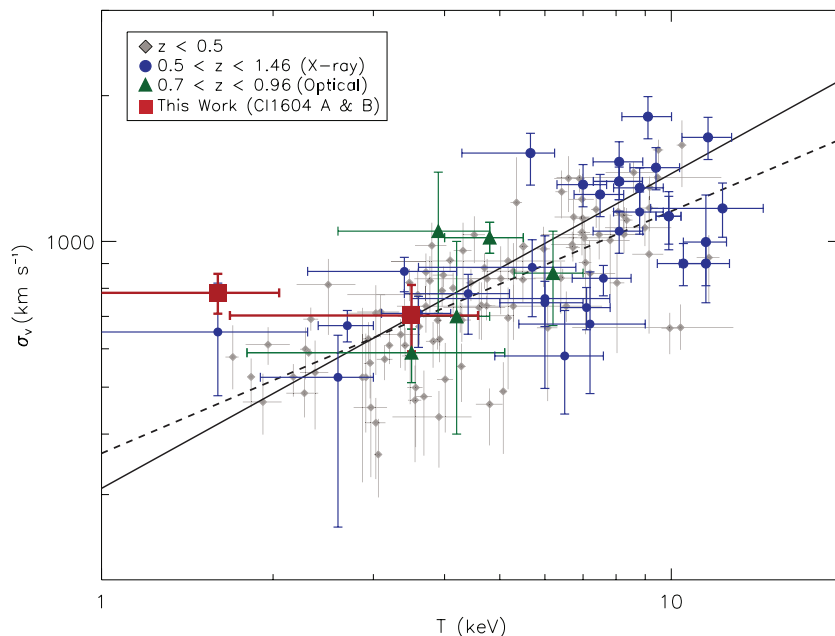


Figure 13. Relation between galaxy velocity dispersion and ICM temperature. The filled squares indicate the two optically selected clusters detected in the Cl1604 Supercluster, while the circles and triangles denote X-ray and optically selected, high-redshift clusters, respectively, drawn from the literature. Diamonds indicate the $z < 0.5$ sample from Horner (2001). The dashed line is the best-fit relation of Horner (2001) to the low-redshift cluster data, while the solid line is that of Xue & Wu (2000).

As our spectral fits for cluster B found it highly unlikely that the system's temperature is significantly greater than 2 keV, which would place the system squarely in-line with the L_x-T relation, an alternative explanation for the observed deviation is that the system is not fully relaxed. In that case the assumption that the ICM shares the same dynamics as the cluster galaxies may not hold true. Gal et al. (2008) note that the redshift distribution for cluster B does show evidence of velocity segregation indicative of either a substructure or a triaxial system. They also find that the velocity dispersions of the red versus blue galaxy populations in the cluster differ by less than

1σ , unlike the 3.7σ difference observed in cluster A. The latter is the most isolated cluster in the Cl1604 supercluster with the most prominent red sequence. If the system formed at an earlier epoch than cluster B, it is expected that the primordial red-galaxy population would have had more time to fully virialize and establish a much different dispersion than any infalling blue galaxy population. The lack of a significant difference in the velocity dispersions of blue and red galaxies in cluster B may be further evidence that the system is undergoing collapse or possible merger processes, which may drive the cluster off the σ_v-T relationship.

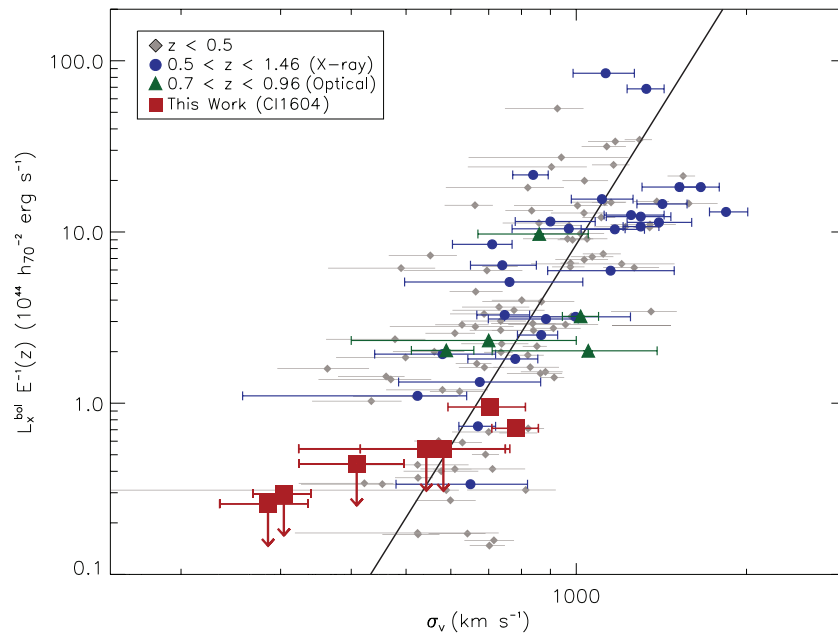


Figure 14. Relation between bolometric luminosity and galaxy velocity dispersion. The filled squares indicate the two optically selected clusters detected in the CI1604 Supercluster, while the circles and triangles denote X-ray and optically selected, high-redshift clusters, respectively, drawn from the literature. Diamonds indicate the $z < 0.5$ sample from Horner (2001). The solid line represents the best-fit relation of Xue & Wu (2000) to the correlation observed in low-redshift clusters.

4.1.3. The L_x - σ_v Relation

In addition to the findings of L04, Fang et al. (2007) have reported that their optically selected clusters detected in the DEEP2 Galaxy Redshift Survey (Davis et al. 2003) are underluminous relative to their measured velocity dispersions. It is expected that the luminosity of the ICM should scale with galaxy velocity dispersion as $L_x \propto \sigma_v^4$ if both the gas and galaxies are in virial equilibrium and if the gas mass is proportional to the virial mass of the system (Quintana & Melnick 1982). The L04 and Fang et al. (2007) results seem to suggest that optical selection of cluster may preferentially select young systems that have not built up a significant ICM and are therefore underluminous compared to X-ray-selected systems.

In Figure 14, we plot the bolometric luminosity of the two detected CI1604 clusters against their measured velocity dispersions. We have also plotted the upper limits obtained for each system in the supercluster that went undetected, but for which we have measured velocity dispersions of galaxies within $1 h_{70}^{-1}$ Mpc of the cluster centers. Also shown are several high-redshift X-ray and optically selected clusters drawn from the literature which have published velocity dispersions. Having corrected for the expected self-similar evolution, we compare the high-redshift observations with the best-fit local relationship of Xue & Wu (2000) and the low-redshift sample of Horner (2001). Using our revised velocity dispersion for cluster A, we find that the system is fully consistent with the L_x - σ_v relation. The same is true for the clusters which we did not detect in our observations given the upper limits on their X-ray luminosities. Cluster B exhibits the greatest deviation (at the 2.6σ level), but given the observed scatter about the best-fit, we conclude that the system is consistent with the relationship.

From our results and those of other optically selected cluster surveys summarized in Figure 14, we conclude that we do not observe a systematic deviation of optically selected clusters from the L_x - σ_v relation. Regarding the deviation observed by Fang et al. (2007), we simply point out that the systems

that deviated most significantly from the L_x - σ_v relation were also the systems whose velocity dispersions were determined using as few as three member galaxies. Given the challenges of measuring accurate velocity dispersions at high redshift with dozens of redshifts (see discussion in Gal et al. 2008), we feel these clusters require further observations before it can be conclusively determined whether they fall significantly off the L_x - σ_v relationship.

5. CONCLUSIONS

We have presented the results of *Chandra* observations of the CI1604 supercluster at $z = 0.9$, the largest such structure mapped at redshifts approaching unity, with the most constituent clusters and groups and the largest number of spectroscopically confirmed member galaxies. Over nearly two ACIS-I pointings, we find a 2.5σ excess of X-ray point sources in the hard₁₀ band, while no such overdensity is observed in the soft band. At a flux of 1×10^{-14} erg s⁻¹ cm⁻² (2–10 keV), the surface density of hard sources is 1.47 times greater than that of a blank field, in excellent agreement with the correlation between cluster redshift and source overdensity observed by Cappelluti et al. (2005). Unlike many previous reports, the overdensity persists when integrated over nearly two full ACIS-I pointings, making it unlikely that the excess is solely due to statistical fluctuations in the source counts. If the excess sources are tracing substructure within the CI1604 system, then this observation supports the notion that more obscured, harder X-ray sources are more highly biased tracers of large-scale structure than their softer counterparts.

Using a maximum likelihood technique, we have matched 112 of the 161 detected X-ray point sources to optical counterparts found in our Palomar 5m-LFC and *HST*/ACS imaging, of which 42 have spectroscopic information available. We find 15 sources that are associated with the supercluster, all of which have rest-frame luminosities consistent with emission from AGN activity. The supercluster AGNs largely avoid the

densest regions of the system and are instead distributed on the outskirts of massive clusters or within poorer clusters and groups. We find a large fraction of the AGNs in or near cluster C. The system has a modest velocity dispersion ($\sigma = 386 \text{ km s}^{-1}$) and we do not detect diffuse emission from the system in these observations. Despite the high density of galaxies in cluster A and extensive spectroscopic coverage of the system, we find no AGNs in or near the cluster. On the other hand, sources are found on the outskirts of cluster B, which has an equally high velocity dispersion and a luminous ICM. The primary difference between the two clusters noted by Gal et al. (2008) is that cluster A appears fully relaxed, while cluster B shows signs of velocity substructure indicative of a recent merger or a significant population of actively accreting galaxies. It is possible that more complex dynamical state of cluster B leads to increased galaxy interactions and/or mergers on the outskirts of the system which may trigger enhanced AGN activity.

We have detected diffuse emission from clusters A and B, while the remaining five clusters and groups in the supercluster show no significant emission above the background. We find that clusters A and B have bolometric luminosities of 1.43×10^{44} and $8.20 \times 10^{43} h_{70}^{-2} \text{ erg s}^{-1}$ and gas temperatures of $3.50_{-1.08}^{+1.82}$ and $1.64_{-0.45}^{+0.65} \text{ keV}$, respectively. Using updated velocity dispersions from Gal et al. (2008), we find that the properties of cluster A agree well with both X-ray–X-ray and X-ray–optical cluster scaling relations followed by high-redshift, X-ray-selected galaxy clusters. On the other hand, we find that clusters B deviates from the σ_v – T relationship at the $\sim 4\sigma$ level. This may be due to the system’s complex dynamical state, indicating that the cluster is not fully relaxed and may still be in the process of forming.

We thank Patrick Henry and Harald Ebeling for several useful discussions. This work is supported by the *Chandra* General Observing Program under award number GO6-7114X. Additional support for this program was provided by NASA through a grant *HST-GO-11003* from the Space Telescope Science Institute, which is operated by the Association of Universities for Research in Astronomy, Inc., under NASA contract NAS 5-26555. The spectrographic data used herein were obtained at the W. M. Keck Observatory, which is operated as a scientific partnership among the California Institute of Technology, the University of California, and the National Aeronautics and Space Administration. The Observatory was made possible by the generous financial support of the W. M. Keck Foundation.

REFERENCES

- Bahcall, N. A., & Soneira, R. M. 1984, *ApJ*, 277, 27
- Barnes, J. E., & Hernquist, L. E. 1991, *ApJ*, 370, L65
- Basilakos, S., Georgakakis, A., Plionis, M., & Georgantopoulos, I. 2004, *ApJ*, 607, L79
- Bauer, F. E., Alexander, D. M., Brandt, W. N., Hornschemeier, A. E., Vignali, C., Garmire, G. P., & Schneider, D. P. 2002, *AJ*, 124, 2351
- Bertin, E., & Arnouts, S. 1996, *A&AS*, 117, 393
- Borgani, S., Rosati, P., Tozzi, P., & Norman, C. 1999, *ApJ*, 517, 40
- Branchesi, M., Gioia, I. M., Fanti, C., Fanti, R., & Cappelluti, N. 2007, *A&A*, 462, 449
- Brandt, W. N., & Hasinger, G. 2005, *ARA&A*, 43, 827
- Brandt, W. N., et al. 2001, *AJ*, 122, 2810
- Cappelluti, N., Cappi, M., Dadina, M., Malaguti, G., Branchesi, M., D’Elia, V., & Palumbo, G. G. C. 2005, *A&A*, 430, 39
- Cappelluti, N., et al. 2007, *ApJS*, 172, 341
- Cappi, M., et al. 2001, *ApJ*, 548, 624
- Castander, F. J., Ellis, R. S., Frenk, C. S., Dressler, A., & Gunn, J. E. 1994, *ApJ*, 424, L79
- Colberg, J. M., et al. 2000, *MNRAS*, 319, 209
- Cowie, L. L., Garmire, G. P., Bautz, M. W., Barger, A. J., Brandt, W. N., & Hornschemeier, A. E. 2002, *ApJ*, 566, L5
- Crawford, D. F., Jauncey, D. L., & Murdoch, H. S. 1970, *ApJ*, 162, 405
- Davis, M., et al. 2003, in SPIE Conf. Ser. 4834, Discoveries and Research Prospects from 6- to 10-Meter-Class Telescopes II, ed. P. Guhathakurta & Puragra (Bellingham, WA: SPIE), 161–172
- D’Elia, V., Fiore, F., Elvis, M., Cappi, M., Mathur, S., Mazzotta, P., Falco, E., & Cocchia, F. 2004, *A&A*, 422, 11
- Demarco, R., et al. 2007, *ApJ*, 663, 164
- Dickey, J. M., & Lockman, F. J. 1990, *ARA&A*, 28, 215
- Donahue, M., Voit, G. M., Scharf, C. A., Gioia, I. M., Mullis, C. R., Hughes, J. P., & Stocke, J. T. 1999, *ApJ*, 527, 525
- Ebeling, H., Barrett, E., Donovan, D., Ma, C.-J., Edge, A. C., & van Speybroeck, L. 2007, *ApJ*, 661, L33
- Ebeling, H., Edge, A. C., & Henry, J. P. 2001a, *ApJ*, 553, 668
- Ebeling, H., Jones, L. R., Fairley, B. W., Perlman, E., Scharf, C., & Horner, D. 2001b, *ApJ*, 548, L23
- Einasto, M., Einasto, J., Tago, E., Müller, V., & Andernach, H. 2001, *AJ*, 122, 2222
- Evrard, A. E., et al. 2002, *ApJ*, 573, 7
- Faber, S. M., et al. 2003, in SPIE Conf. Ser. 4841, Instrument Design and Performance for Optical/Infrared Ground-Based Telescopes, ed. M. Iye & A. F. M. Moorwood (Bellingham, WA: SPIE), 1657–1669
- Fang, T., et al. 2007, *ApJ*, 660, L27
- Freeman, P. E., Kashyap, V., Rosner, R., & Lamb, D. Q. 2002, *ApJS*, 138, 185
- Gal, R. R., Lemaux, B. C., Lubin, L. M., Kocevski, D., & Squires, G. K. 2008, *ApJ*, 684, 933
- Gal, R. R., & Lubin, L. M. 2004, *ApJ*, 607, L1
- Gal, R. R., Lubin, L. M., & Squires, G. K. 2005, *AJ*, 129, 1827
- Garmire, G. P., Bautz, M. W., Ford, P. G., Nousek, J. A., & Ricker Jr., G. R. 2003, in SPIE Conf. Ser. 4851, X-Ray and Gamma-Ray Telescopes and Instruments for Astronomy, ed. J. E. Truemper & H. D. Tananbaum (Bellingham, WA: SPIE), 28–44
- Gehrels, N. 1986, *ApJ*, 303, 336
- Gilbank, D. G., Yee, H. K. C., Ellingson, E., Hicks, A. K., Gladders, M. D., Barrientos, L. F., & Keeney, B. 2008, *ApJL*, 677, 89
- Gilli, R., et al. 2005, *A&A*, 430, 811
- Gilmour, R., Gray, M. E., Almaini, O., Best, P., Wolf, C., Meisenheimer, K., Papovich, C., & Bell, E. 2007, *MNRAS*, 380, 1467
- Gioia, I. M., Henry, J. P., Mullis, C. R., Ebeling, H., & Wolter, A. 1999, *AJ*, 117, 2608
- Gioia, I. M., Maccacaro, T., Schild, R. E., Wolter, A., Stocke, J. T., Morris, S. L., & Henry, J. P. 1990, *ApJS*, 72, 567
- Gladders, M. D., & Yee, H. K. C. 2005, *ApJS*, 157, 1
- Gómez, P. L., et al. 2003, *ApJ*, 584, 210
- Gunn, J. E., Hoessel, J. G., & Oke, J. B. 1986, *ApJ*, 306, 30
- Henry, J. P., & Briel, U. G. 1991, *A&A*, 246, L14
- Hicks, A. K., Ellingson, E., Hoekstra, H., & Yee, H. K. C. 2006, *ApJ*, 652, 232
- Hicks, A. K., et al. 2007, *ApJ*, 680, 1022
- Hilton, M., et al. 2007, *ApJ*, 670, 1000
- Holden, B. P., et al. 2001, *AJ*, 122, 629
- Horner, D. J. 2001, PhD thesis, Univ. Maryland College Park
- Hudaverdi, M., Kunieda, H., Tanaka, T., Haba, Y., Furuzawa, A., Tawara, Y., & Ercan, E. N. 2006, *PASJ*, 58, 931
- Johnson, O., Best, P. N., & Almaini, O. 2003, *MNRAS*, 343, 924
- Johnson, O., et al. 2006, *MNRAS*, 371, 1777
- Kaiser, N. 1986, *MNRAS*, 222, 323
- Kim, D.-W., et al. 2004a, *ApJS*, 150, 19
- Kim, D.-W., et al. 2004b, *ApJ*, 600, 59
- Kim, M., et al. 2007, *ApJS*, 169, 401
- Kushino, A., Ishisaki, Y., Morita, U., Yamasaki, N. Y., Ishida, M., Ohashi, T., & Ueda, Y. 2002, *PASJ*, 54, 327
- Lewis, I., et al. 2002, *MNRAS*, 334, 673
- Lubin, L. M., Brunner, R., Metzger, M. R., Postman, M., & Oke, J. B. 2000, *ApJ*, 531, L5
- Lubin, L. M., Mulchaey, J. S., & Postman, M. 2004, *ApJ*, 601, L9
- Lubin, L. M., Postman, M., Oke, J. B., Ratnatunga, K. U., Gunn, J. E., Hoessel, J. G., & Schneider, D. P. 1998, *AJ*, 116, 584
- Markevitch, M. 1998, *ApJ*, 504, 27
- Martini, P., Kelson, D. D., Kim, E., Mulchaey, J. S., & Athey, A. A. 2006, *ApJ*, 644, 116
- Martini, P., Kelson, D. D., Mulchaey, J. S., & Trager, S. C. 2002, *ApJ*, 576, L109

- Maughan, B. J., Jones, L. R., Ebeling, H., & Scharf, C. 2004, *MNRAS*, **351**, 1193
- Maughan, B. J., Jones, L. R., Ebeling, H., & Scharf, C. 2006, *MNRAS*, **365**, 509
- Miyaji, T., et al. 2007, *ApJS*, **172**, 396
- Molnar, S. M., Hughes, J. P., Donahue, M., & Joy, M. 2002, *ApJ*, **573**, L91
- Monet, D. G., et al. 2003, *AJ*, **125**, 984
- Moore, B., Katz, N., Lake, G., Dressler, A., & Oemler, A. 1996, *Nature*, **379**, 613
- Mullis, C. R., Rosati, P., Lamer, G., Böhringer, H., Schwobe, A., Schuecker, P., & Fassbender, R. 2005, *ApJ*, **623**, L85
- Murdoch, H. S., Crawford, D. F., & Jauncey, D. L. 1973, *ApJ*, **183**, 1
- Nakata, F., Kodama, T., Shimasaku, K., Doi, M., Furusawa, H., Hamabe, M., Kimura, M., & Komiyama, Y. 2005, *MNRAS*, **357**, 1357
- Oke, J. B., Postman, M., & Lubin, L. M. 1998, *AJ*, **116**, 549
- Oke, J. B., et al. 1995, *PASP*, **107**, 375
- Pentericci, L., Kurk, J. D., Carilli, C. L., Harris, D. E., Miley, G. K., & Röttgering, H. J. A. 2002, *A&A*, **396**, 109
- Postman, M., Lubin, L. M., & Oke, J. B. 1998, *AJ*, **116**, 560
- Postman, M., Lubin, L. M., & Oke, J. B. 2001, *AJ*, **122**, 1125
- Quintana, H., & Melnick, J. 1982, *AJ*, **87**, 972
- Rosati, P., et al. 2002, *ApJ*, **566**, 667
- Rosati, P., et al. 2004, *AJ*, **127**, 230
- Ruderman, J. T., & Ebeling, H. 2005, *ApJ*, **623**, L81
- Rutledge, R. E., Brunner, R. J., Prince, T. A., & Lonsdale, C. 2000, *ApJS*, **131**, 335
- Scoville, N., et al. 2007, *ApJS*, **172**, 1
- Shapley, H. 1930, *Harv. Coll. Obs. Bull.*, **874**, 9
- Stanford, S. A., Holden, B., Rosati, P., Eisenhardt, P. R., Stern, D., Squires, G., & Spinrad, H. 2002, *AJ*, **123**, 619
- Stanford, S. A., Holden, B., Rosati, P., Tozzi, P., Borgani, S., Eisenhardt, P. R., & Spinrad, H. 2001, *ApJ*, **552**, 504
- Sutherland, W., & Saunders, W. 1992, *MNRAS*, **259**, 413
- Swinbank, A. M., et al. 2007, *MNRAS*, **379**, 1343
- Taylor, E. L., et al. 2005, *MNRAS*, **361**, 1352
- Tozzi, P., et al. 2001, *ApJ*, **562**, 42
- Tran, K.-V. H., Kelson, D. D., van Dokkum, P., Franx, M., Illingworth, G. D., & Magee, D. 1999, *ApJ*, **522**, 39
- Tully, R. B., Scaramella, R., Vettolani, G., & Zamorani, G. 1992, *ApJ*, **388**, 9
- Valtchanov, I., et al. 2004, *A&A*, **423**, 75
- Vikhlinin, A., van Speybroeck, L., Markevitch, M., Forman, W. R., & Grego, L. 2002, *ApJ*, **578**, L107
- White, S. D. M., et al. 2005, *A&A*, **444**, 365
- Xue, Y.-J., & Wu, X.-P. 2000, *ApJ*, **538**, 65
- Yang, Y., Mushotzky, R. F., Barger, A. J., & Cowie, L. L. 2006, *ApJ*, **645**, 68
- Yang, Y., Mushotzky, R. F., Barger, A. J., Cowie, L. L., Sanders, D. B., & Steffen, A. T. 2003, *ApJ*, **585**, L85